GEOPHYSICS, VOL. 74, NO. 5 (SEPTEMBER-OCTOBER 2009); P. T75–T95, 16 FIGS., 3 TABLES.
10.1190/1.3157243

Finite-difference frequency-domain modeling of viscoacoustic wave propagation in 2D tilted transversely isotropic (TTI) media

Stéphane Operto[1], Jean Virieux[2], A. Ribodetti[1], and J. E. Anderson[3]

ABSTRACT

A 2D finite-difference, frequency-domain method was developed for modeling viscoacoustic seismic waves in transversely isotropic media with a tilted symmetry axis. The medium is parameterized by the P-wave velocity on the symmetry axis, the density, the attenuation factor, Thomsen's anisotropic parameters δ and ϵ, and the tilt angle. The finite-difference discretization relies on a parsimonious mixed-grid approach that designs accurate yet spatially compact stencils. The system of linear equations resulting from discretizing the time-harmonic wave equation is solved with a parallel direct solver that computes monochromatic wavefields efficiently for many sources. Dispersion analysis shows that four grid points per P-wavelength provide sufficiently accurate solutions in homogeneous media. The absorbing boundary conditions are perfectly matched layers (PMLs). The kinematic and dynamic accuracy of the method was assessed with several synthetic examples which illustrate the propagation of S-waves excited at the source or at seismic discontinuities when $\epsilon < \delta$. In frequency-domain modeling with absorbing boundary conditions, the unstable S-wave mode is not excited when $\epsilon < \delta$, allowing stable simulations of the P-wave mode for such anisotropic media. Some S-wave instabilities are seen in the PMLs when the symmetry axis is tilted and $\epsilon > \delta$. These instabilities are consistent with previous theoretical analyses of PMLs in anisotropic media; they are removed if the grid interval is matched to the P-wavelength that leads to dispersive S-waves. Comparisons between seismograms computed with the frequency-domain acoustic TTI method and a finite-difference, time-domain method for the vertical transversely isotropic elastic equation show good agreement for weak to moderate anisotropy. This suggests the method can be used as a forward problem for viscoacoustic anisotropic full-waveform inversion.

INTRODUCTION

It is well acknowledged that accounting for anisotropy in depth seismic imaging can improve reservoir delineation in oil and gas exploration. Anisotropic seismic imaging generally relies on the assumption of vertical transverse isotropy (VTI), which can provide a good representation of intrinsic anisotropy of shales in sedimentary basins (Tsvankin, 2001). More complex tectonic environments involving dipping structures such as foothills and overthrust areas need to account for a tilted symmetry axis in transversely isotropic (TTI) media (Boudou et al., 2007; Charles et al., 2008). Deep crustal exploration using long-offset acquisition surveying is another context where anisotropy can significantly influence the seismic data as waves recorded by this acquisition design travel with a broad range of incidence angles (Jones et al., 1999; Okaya and McEvelly, 2003).

We present a 2D finite-difference, frequency-domain (FDFD) method to model seismic wave propagation in viscoacoustic transversely isotropic media with arbitrary tilted symmetry axis. Our motivation behind this modeling method is to introduce anisotropy into the frequency-domain viscoacoustic full-waveform inversion (FWI) of wide-aperture seismic data.

Over the last decade, frequency-domain FWI has been acknowledged as a promising approach to build high-resolution velocity models in complex environments (Pratt and Shipp, 1999; Ravaut et al., 2004; Brenders and Pratt, 2007b). Frequency-domain FWI is based on the full (two-way) wave equation that needs to be solved for many sources at each inversion iteration. Therefore, a computationally efficient modeling tool is a central ingredient for 2D and 3D FWIs that are tractable on distributed-memory platforms.

Manuscript received by the Editor 20 October 2008; revised manuscript received 3 April 2009; published online 27 August 2009.
[1]Université de Nice Sophia-Antipolis, Géosciences Azur, Villefranche-sur-mer, France. E-mail: operto@geoazur.obs-vlfr.fr; ribodeti@geoazur.obs-vlfr.fr.
[2]Université Joseph Fourier, Laboratoire de Géophysique Interne et Tectonophysique, Grenoble, France. E-mail: jean.virieux@obs.ujf-grenoble.fr.
[3]ExxonMobil, Houston, Texas, U.S.A. E-mail: john.e.anderson1@exxonmobil.com.

Multiscale frequency-domain FWI generally is performed by successive inversions of a limited subset of frequencies, proceeding from low frequencies to higher ones (Sirgue and Pratt, 2004; Brenders and Pratt, 2007a). In two dimensions, these few frequencies can be modeled efficiently in the frequency domain. Frequency-domain wave modeling reduces to the resolution of a large, sparse system of linear equations, the solution for which is a monochromatic wavefield with the right-hand-side term as the source. The most efficient computational approach to solve this system for a large number of right-hand-side terms is to perform one LU factorization of the impedance matrix with a direct solver, followed by forward/backward substitutions for each right-hand-side term (see Marfurt [1984] and Nihei and Li [2007] for a comparison between time and memory complexities of time-domain and frequency-domain modeling approaches). Parallel frequency-domain modeling is performed by using a massively parallel direct solver that reduces the computing cost of the factorization by over an order of magnitude (Operto et al., 2007b; Sourbier et al., 2009a, 2009b).

Compact mixed-grid, finite-difference stencils with antilumped mass have been developed specifically for 2D and 3D frequency-domain modeling based on a direct solver to minimize the memory requirement of LU factorization (Jo et al., 1996; Stekl and Pratt, 1998; Hustedt et al., 2004; Operto et al., 2007b). Massively parallel FWI algorithms based on this forward-modeling approach are presented in Sourbier et al. (2009a, 2009b) and Ben Hadj Ali et al. (2008). The frequency domain also allows the implementation of attenuation effects of arbitrary complexity without extra computational effort by using complex velocities (Toksöz and Johnston, 1981).

We extend the viscoacoustic isotropic modeling method of Hustedt et al. (2004) to a viscoacoustic TTI wave equation. A fourth-order acoustic wave equation for VTI media was originated by Alkhalifah (2000). The wave equation is derived from the exact expression of the phase velocity within which the S-wave velocity on the symmetry axis is set to zero. Alkhalifah (2000) shows that his acoustic VTI wave equation is accurate kinematically for P-wave propagation. Zhang et al. (2005) extend his equation to consider acoustic TTI media. They illustrate the effects of the tilt of the symmetry axis on the kinematics of the arrivals by comparing VTI and TTI seismograms with an explicit high-order, finite-difference time-domain (FDTD) method. Zhou et al. (2006) extend Alkhalifah's equation to the TTI case and recast the resulting fourth-order equation into a coupled system of second-order partial differential equations; these are more suitable for numerical implementation and are easier to interpret from a physical viewpoint. This system of equations is implemented with a classic FDTD method, and some simulations in homogeneous media are presented.

Several limitations of the acoustic anisotropic wave equation of Alkhalifah (2000) can be identified. His wave equation does not describe any physically realizable phenomenon because acoustic media intrinsically are isotropic. Rather, Alkhalifah's (2000) equation is derived by setting the S-wave velocity on the symmetry axis V_{S_0} to zero in the expression of the phase velocity for VTI media. This condition does not prevent the propagation of S-waves out of the symmetry axis (Grechka et al., 2004; Zhang et al., 2005), and these S-waves must be regarded as artifacts in the framework of acoustic modeling. The fact that shear waves are propagated means that his equation cannot be considered as acoustic in the strict sense of the word.

During numerical modeling, S-waves are excited at seismic sources located in a VTI or TTI layer or can be converted from the P-mode at interfaces. These shear waves are not excited in elliptical anisotropic media. Furthermore, acoustic VTI media characterized by $\epsilon < \delta$ do not satisfy the stability condition for hexagonal symmetry given by $C_{33}C_{11} - C_{13}^2 > 0$ when $\epsilon < \delta$ and C_{ij} are the elastic moduli (Helbig, 1994; p. 191). The analytical solutions of the VTI equation show that one mode is unstable when $\epsilon < \delta$ (Alkhalifah, 2000; his equations 20–21 and his Figure 1); the phase velocity of the S-wave mode, which becomes imaginary when $\epsilon < \delta$, strongly suggests that the unstable mode is the undesired S-wave mode (Grechka et al., 2004; their equations 1 and 5). Therefore, time-domain anisotropic acoustic modeling based on the full solution of the wave equation has been limited to acoustic VTI media characterized by $\epsilon > \delta$.

Of note, the undesired S-wavefield can be separated from the P-wavefield in the phase-shift extrapolation method because the P- and S-wave solutions lie in a different part of the wavenumber spectrum (Bale, 2007). The unstable S-wave mode can be cancelled out when $\epsilon < \delta$ by choosing the sign of the phase-shift operator that guarantees evanescent decay of the S-waves. Thus, numerically stable simulation of the P-wavefield can be performed with a phase-shift extrapolation method when $\epsilon < \delta$ (Bale, 2007).

Whereas the acoustic anisotropic wave equation is sufficiently kinematically accurate to perform prestack depth and reverse-time migration in anisotropic media (see Duveneck et al. [2008] for a recent example), amplitude modeling appears to be inaccurate, although to our knowledge no numerical studies quantify this level of inaccuracy.

In this paper, we implement the equation of Zhou et al. (2006) in the frequency domain rather than in the time domain for efficient multisource modeling of monochromatic wavefields. In a first attempt to incorporate anisotropy in FWI, we consider a viscoacoustic TTI wave equation rather than an elastic one with more general representation of anisotropy (Carcione et al., 1992; Komatitsch et al., 2000; Saenger and Bohlen, 2004). The first obvious reason is that elastic modeling is more demanding than acoustic, among others, because the elastic wave equation is discretized according to the minimum S-wavelength, leading to a finer grid interval than in the acoustic case. The second motivation is to deal with a more limited number of parameter classes in FWI to manage the ill-posedness of the inverse problem. In this paper, the viscoacoustic anisotropic medium is parameterized by the P-wave velocity on the symmetry axis, the density, the attenuation factor, the anisotropic parameters ϵ and δ, and the tilt angle, which is not supposed constant in the medium. Elliptic anisotropy can be considered easily by setting $\epsilon = \delta$, further decreasing the number of independent parameters if necessary.

In the next section, we review the TTI acoustic wave equation of Zhou et al. (2006) and extend it to incorporate heterogeneous density. Following that, we discretize the TTI acoustic wave equation with the FDFD method. Perfectly matched layers (PMLs) are used as absorbing boundary conditions (Berenger, 1994). Some instabilities of the PMLs in the TTI case are highlighted. The source implementation is then discussed to find a way to attenuate the excitation of the S-waves. In the fourth section, we present a dispersion analysis in homogeneous media, which shows that four grid points per

P-wavelength provide sufficiently accurate simulations in homogenous media. In the fifth section, the numerical simulations provide insight into the kinematic and dynamic accuracy of the acoustic TTI wave equation in comparison with the elastic wave equation. We conclude with a discussion of the reliability of the anisotropic acoustic wave equation for performing anisotropic FWI.

THE TTI ACOUSTIC WAVE EQUATION

We start from a modification of the 2D acoustic wave equation of Zhou et al. (2006) for TTI anisotropic media:

$$\begin{cases} \dfrac{1}{\kappa_0}\dfrac{\partial^2 p}{\partial t^2} - (1+2\delta)Hp - H_0 p = (1+2\delta)Hq \\ \dfrac{1}{\kappa_0}\dfrac{\partial^2 q}{\partial t^2} - 2(\epsilon-\delta)Hq = 2(\epsilon-\delta)Hp \end{cases}, \quad (1)$$

with

$$\begin{aligned} H &= \cos^2\theta_0 \frac{\partial}{\partial x} b \frac{\partial}{\partial x} + \sin^2\theta_0 \frac{\partial}{\partial z} b \frac{\partial}{\partial z} \\ &\quad - \frac{\sin 2\theta_0}{2}\left(\frac{\partial}{\partial x} b \frac{\partial}{\partial z} + \frac{\partial}{\partial z} b \frac{\partial}{\partial x}\right), \\ H_0 &= \sin^2\theta_0 \frac{\partial}{\partial x} b \frac{\partial}{\partial x} + \cos^2\theta_0 \frac{\partial}{\partial z} b \frac{\partial}{\partial z} \\ &\quad + \frac{\sin 2\theta_0}{2}\left(\frac{\partial}{\partial x} b \frac{\partial}{\partial z} + \frac{\partial}{\partial z} b \frac{\partial}{\partial x}\right), \end{aligned} \quad (2)$$

where p is the pressure wavefield, q is an auxiliary wavefield introduced by Zhou et al. (2006) to recast the fourth-order equation of Alkhalifah (1998) into the system of second-order equations 1, κ_0 is the bulk modulus along the symmetry axis, and b is buoyancy, the inverse of density. The values δ and ϵ are Thomsen's dimensionless anisotropic parameters (Thomsen, 1986), and θ_0 is the angle of the symmetry axis with respect to the z-axis. Compared to the original equation of Zhou et al. (2006), we introduce heterogeneous buoyancy in operators H and H_0, taking advantage of the analogy of equations 1 and 2 with the isotropic wave equation.

The second equation in the system of equation 1 vanishes in the case of elliptical anisotropy ($\epsilon = \delta$). If $\delta = \epsilon = \theta = 0$, then equation 1 reduces to the second-order acoustic isotropic wave equation, the solution of which is the pressure wavefield. Also of note is that the tilt of the anisotropy introduces some cross-derivative terms in operators H and H_0. The source term of the first expression of equation 1 depends on the q-wavefield, the amplitude of which is controlled by the amount of anellipticity, as revealed by the coefficient $(\epsilon - \delta)$ in the source term of the second expression of equation 1.

We can transform the previous system of second-order equations into a hyperbolic system of first-order equations by introducing auxiliary wavefields p_x, p_z, q_x, and q_z:

$$\begin{cases} \dfrac{1}{\kappa_0}\dfrac{\partial p}{\partial t} = A_x\dfrac{\partial p_x}{\partial x} + B_x\dfrac{\partial p_z}{\partial x} + C_x\dfrac{\partial q_x}{\partial x} + D_x\dfrac{\partial q_z}{\partial x} \\ \qquad + A_z\dfrac{\partial p_x}{\partial z} + B_z\dfrac{\partial p_z}{\partial z} + C_z\dfrac{\partial q_x}{\partial z} + D_z\dfrac{\partial q_z}{\partial z} \\ \dfrac{1}{\kappa_0}\dfrac{\partial q}{\partial t} = E_x\dfrac{\partial p_x}{\partial x} + F_x\dfrac{\partial p_z}{\partial x} + G_x\dfrac{\partial q_x}{\partial x} + H_x\dfrac{\partial q_z}{\partial x} \\ \qquad + E_z\dfrac{\partial p_x}{\partial z} + F_z\dfrac{\partial p_z}{\partial z} + G_z\dfrac{\partial q_x}{\partial z} + H_z\dfrac{\partial q_z}{\partial z} \\ \dfrac{\partial p_x}{\partial t} = b\dfrac{\partial p}{\partial x} \\ \dfrac{\partial p_z}{\partial t} = b\dfrac{\partial p}{\partial z} \\ \dfrac{\partial q_x}{\partial t} = b\dfrac{\partial q}{\partial x} \\ \dfrac{\partial q_z}{\partial t} = b\dfrac{\partial q}{\partial z} \end{cases}, \quad (3)$$

where the coefficients

$$A_x = 1 + 2\delta\cos^2(\theta),\ B_x = -\delta\sin(2\theta),$$

$$C_x = (1+2\delta)\cos^2(\theta),\ D_x = -(1+2\delta)\frac{\sin(2\theta)}{2},$$

$$A_z = B_x,\ B_z = 1 + 2\delta\sin^2(\theta),$$

$$C_z = D_x,\ D_z = (1+2\delta)\sin^2(\theta),$$

$$E_x = 2(\epsilon-\delta)\cos^2(\theta),\ F_x = -(\epsilon-\delta)\sin(2\theta),$$

$$G_x = E_x,\ H_x = F_x,$$

and

$$E_z = F_x, F_z = 2(\epsilon-\delta)\sin^2(\theta),\ G_z = F_x, H_z = F_z \quad (4)$$

can be introduced for compactness. By analogy with the velocity-stress formulation of the isotropic acoustic wave equation (Hustedt et al., 2004), p_x, p_z, q_x, and q_z represent particle velocity wavefields.

We take the Fourier transform with respect to time and introduce 1D damping functions $\xi_x(x)$ and $\xi_z(z)$ for convolutional (C) PML absorbing boundary conditions, e.g. (Drossaert and Giannopoulos, 2007; Komatitsch and Martin, 2007),

$$\begin{cases} \dfrac{-i\omega}{\kappa_0} p &= \dfrac{1}{\xi_x}\left(A_x\dfrac{\partial p_x}{\partial x} + B_x\dfrac{\partial p_z}{\partial x} + C_x\dfrac{\partial q_x}{\partial x} + D_x\dfrac{\partial q_z}{\partial x}\right) \\ &\quad + \dfrac{1}{\xi_z}\left(A_z\dfrac{\partial p_x}{\partial z} + B_z\dfrac{\partial p_z}{\partial z} + C_z\dfrac{\partial q_x}{\partial z} + D_z\dfrac{\partial q_z}{\partial z}\right) \\ \dfrac{-i\omega}{\kappa_0} q &= \dfrac{1}{\xi_x}\left(E_x\dfrac{\partial p_x}{\partial x} + F_x\dfrac{\partial p_z}{\partial x} + G_x\dfrac{\partial q_x}{\partial x} + H_x\dfrac{\partial q_z}{\partial x}\right) \\ &\quad + \dfrac{1}{\xi_z}\left(E_z\dfrac{\partial p_x}{\partial z} + F_z\dfrac{\partial p_z}{\partial z} + G_z\dfrac{\partial q_x}{\partial z} + H_z\dfrac{\partial q_z}{\partial z}\right) \\ -i\omega p_x &= \dfrac{b}{\xi_x}\dfrac{\partial p}{\partial x} \\ -i\omega p_z &= \dfrac{b}{\xi_z}\dfrac{\partial p}{\partial z} \\ -i\omega q_x &= \dfrac{b}{\xi_x}\dfrac{\partial q}{\partial x} \\ -i\omega q_z &= \dfrac{b}{\xi_z}\dfrac{\partial q}{\partial z} \end{cases}. \tag{5}$$

The C-PML function ξ_x has the form $\xi_x = \beta_x + (d_x/(\alpha_x + i\omega))$, where d_x, α_x, and β_x are damping functions, discussed in Komatitsch and Martin (2007) and Drossaert and Giannopoulos (2007). Attenuation effects, including frequency-dependent attenuation, can be implemented easily in equation 5 by making the velocity on the symmetry axis complex (Toksöz and Johnston, 1981).

FDFD DISCRETIZATION

We have discretized equation 5 using the mixed-grid method originally introduced by Jo et al. (1996) and have recast it in the framework of the parsimonious staggered-grid method of Hustedt et al. (2004). The parsimonious mixed-grid method is applied to the 2D and 3D isotropic acoustic wave equations by Hustedt et al. (2004) and Operto et al. (2007b), respectively.

Parsimonious mixed-grid finite-difference method: Principle

Spatial derivatives in the second-order wave equation (such as equation 1) are discretized using $\mathcal{O}(\Delta x^2)$ stencils on different rotated coordinate systems (in two dimensions, the Cartesian axes x and z and the 45° rotated axes). The resulting stencils are combined linearly to derive numerically isotropic stencils. This trick is complemented by a mass-term distribution (an antilumped mass) that significantly improves the accuracy of the mixed-grid stencil (Marfurt, 1984). The linear combination of the stencils of low-order accuracy and the mass distribution allow us to design accurate and spatially compact stencils. This latter feature is crucial to minimize the numerical bandwidth of the impedance matrix and hence its filling during LU factorization.

The $\mathcal{O}(\Delta x^2)$ stencils of the second-order wave equation are designed using a parsimonious staggered-grid method developed for the time-domain wave equation (Luo and Schuster, 1990). In the parsimonious approach, the wave equation is written as a first-order velocity-stress hyperbolic system (such as equation 5) and discretized using $\mathcal{O}(\Delta x^2)$ staggered-grid stencils in the different coordinate systems (Virieux, 1984; Saenger et al., 2000). After discretization, the particle velocities (in the acoustic case) are eliminated from the velocity-stress wave equation, leading to a parsimonious staggered-grid wave equation on each coordinate system, the solution of which is the pressure wavefield. Once discretization and elimination have been applied in each coordinate system, the resulting discrete operators are combined linearly to end up with a single discrete wave equation. A necessary condition for this combination is that the wavefields kept after elimination are discretized in the same grid, whatever the coordinate system selected.

Application to 2D TTI acoustic wave equation

We have applied this discretization strategy to equation 5. The first-order partial derivatives in equation 5 are discretized along the axis of the two coordinate systems (the classic Cartesian one and the 45° rotated one) using $\mathcal{O}(\Delta x^2)$ staggered-grid stencils (Virieux, 1986; Saenger et al., 2000). The resulting stencils are referred to as Cartesian system (CS) and rotated system (RS). After discretization, the auxiliary wavefields p_x, p_z, q_x, and q_z are eliminated from the system to end up with a system of two second-order equations in p and q.

The geometry of the staggered grids for the CS and RS stencils is illustrated in Figure 1. The TTI equation is inconsistent with the geometry of the CS stencil. Indeed, the p- and q-wavefields need to be defined at the four corners and in the middle of the cell because of the cross-derivatives in H and H_0 (Figure 1b). Because we used the $\mathcal{O}(\Delta x^2)$ stencil, we performed bilinear interpolation to estimate the value of p and q in the middle of the cell from their values at the four corners. In contrast, no interpolation is required for the RS stencil because the p- and q-wavefields and the auxiliary wavefields p_x, p_z, q_x, and q_z are defined in the same grid (Figure 1a).

After discretization and linear combination of the two stencils, the system of second-order wave equations can be written in matrix form as

$$\begin{pmatrix} M_p + w_1A_r + (1-w_1)A_c & w_1B_r + (1-w_1)B_c \\ w_1C_r + (1-w_1)C_c & M_q + w_1D_r + (1-w_1)D_c \end{pmatrix} \times \begin{pmatrix} p \\ q \end{pmatrix} = \begin{pmatrix} 0 \\ 0 \end{pmatrix}, \tag{6}$$

where M_p denotes the diagonal mass matrix of coefficients ω^2/κ_0. Blocks A_r, B_r, C_r, D_r and A_c, B_c, C_c, D_c form the stiffness matrices for the RS and CS stencils, respectively. The coefficient w_1 controls the respective weight of the two stencils; it is determined during dispersion analysis by minimizing the phase-velocity dispersion. The mixed-grid stencil contains nine coefficients spanning over two grid intervals (Figure 2; Appendices A and B). This implies that each of the four $(nx \times nz)^2$ blocks of the matrix in equation 6 has nine nonzero coefficients per row. The symmetric band-diagonal pattern of each submatrix is the same as that shown by Hustedt et al. (2004) for the isotropic acoustic wave equation (Hustedt et al., 2004; their Figure 10a). In the case of elliptic anisotropy, the q-wavefield is nil; therefore, only the upper-left block remains in equation 8.

The coefficients of submatrices A_r, B_r, C_r, and D_r are given in Appendix A; those of submatrices A_c, B_c, C_c, and D_c are given in Appendix B.

Antilumped mass

One can also introduce a mass term averaging over the nine grid points of the mixed-grid stencil to improve stencil accuracy. The diagonal term of the mass matrices is replaced by its weight average (Stekl and Pratt, 1998):

$$\frac{\omega^2}{\kappa_{ij}} \rightarrow w_{m1}\frac{\omega^2}{\kappa_{ij}} + \frac{w_{m2}}{4}\left(\frac{\omega^2}{\kappa_{i+1,j}} + \frac{\omega^2}{\kappa_{i-1,j}} + \frac{\omega^2}{\kappa_{i,j+1}} + \frac{\omega^2}{\kappa_{i,j-1}}\right) + \frac{(1-w_{m1}-w_{m2})}{4}\left(\frac{\omega^2}{\kappa_{i+1,j+1}} + \frac{\omega^2}{\kappa_{i-1,j-1}} + \frac{\omega^2}{\kappa_{i-1,j+1}} + \frac{\omega^2}{\kappa_{i+1,j-1}}\right), \quad (7)$$

where we introduce two new mass coefficients w_{m1} and w_{m2}, determined jointly with w_1 during the dispersion analysis.

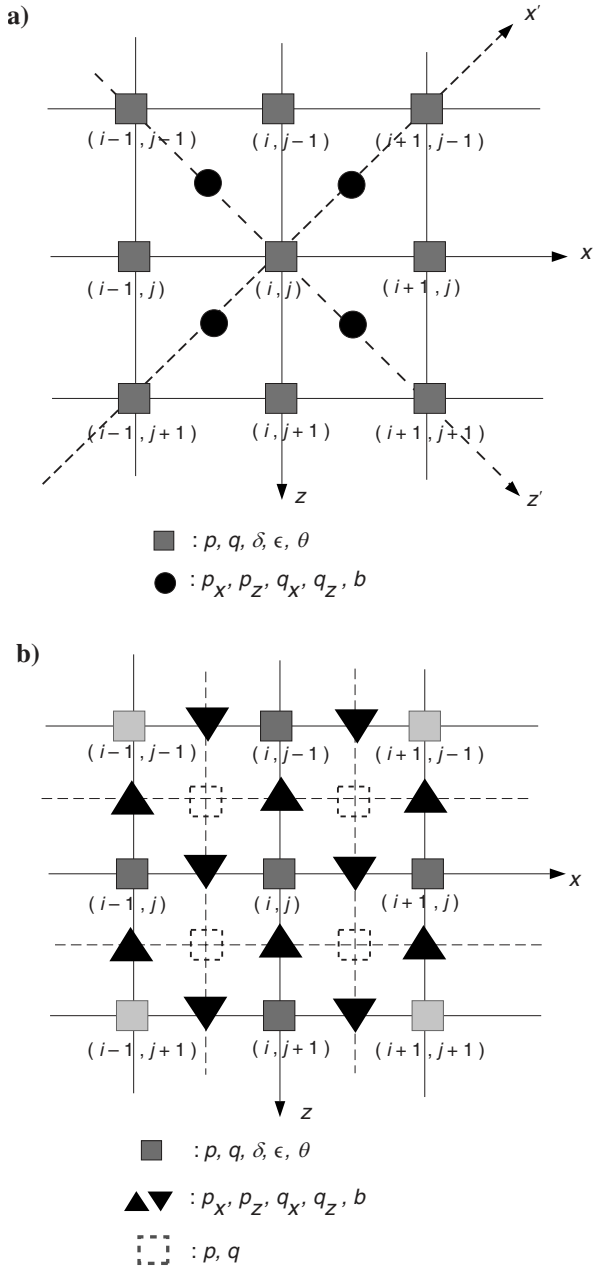

Figure 1. Staggered-grid geometries. (a) RS staggered-grid stencils. (b) CS staggered-grid stencils. The CS stencil requires estimating the p- and q-wavefields in the middle of the cell (dash squares). These are estimated by bilinear interpolation using the values at the four nodes of the cell.

DISPERSION ANALYSIS

To assess the accuracy of the mixed-grid stencil, we perform a classical harmonic dispersion analysis for infinite homogeneous media. This dispersion analysis is applied to the RS, CS, and mixed-grid stencils.

We insert the following discrete plane wave in the discrete wave equation for a homogeneous medium:

$$\begin{pmatrix} p \\ q \end{pmatrix} = \begin{pmatrix} P \\ Q \end{pmatrix} e^{ikh(m\cos\phi + n\sin\phi)} \quad (8)$$

Here, $k = \omega/c_{P_0}$ is the wavenumber, h is the grid interval, ϕ is the in-

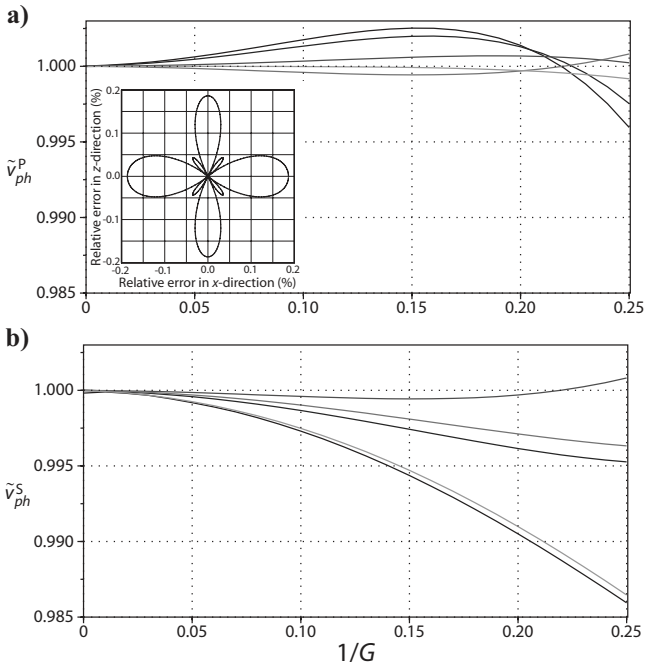

Figure 2. Normalized phase velocity as a function of the number of grid points per wavelength for the (a) P-wave and (b) S-wave modes. The dispersion curves are computed with the mixed-grid stencil for propagation angles of 0°, 15°, 30°, 45°, 60°, and 75° and for Thomsen's parameters $\delta = 0.1$ and $\epsilon = 0.25$. The inset in (a) shows the relative error in percentages of the P-wave phase velocity for $G = 5$, i.e., $(\tilde{v}^{P}_{\text{phase}} - 1) \times 100$ (see text for details). The maximum error is less than 0.2%.

cidence angle of the plane wave, $x = mh$, and $z = nh$. This leads to a system of equations in P and Q of the form

$$\left[\begin{pmatrix} \frac{\omega^2}{c_{P_0}^2} & 0 \\ 0 & \frac{\omega^2}{c_{P_0}^2} \end{pmatrix} + \left(\frac{kG}{2\pi}\right)^2 \underbrace{\begin{pmatrix} a_{11} & a_{12} \\ a_{21} & a_{22} \end{pmatrix}}_{\mathcal{M}}\right]\begin{pmatrix} P \\ Q \end{pmatrix} = \begin{pmatrix} 0 \\ 0 \end{pmatrix}, \tag{9}$$

where the expression of the coefficients a_{11}, a_{12}, a_{21}, and a_{22} are given in Appendix C for the RS and CS stencils; G denotes the number of grid points per wavelength, $G = 2\pi/kh$.

The two eigenvalues $e = -\omega^2/c_{P_0}^2$ of the matrix $\mathcal{M}$ are provided by the roots of the characteristic polynomial $\det(\mathcal{M} - e\mathbf{I}) = 0$. We can infer from their expressions the numerical phase velocities of the two modes:

$$\begin{aligned} v_{ph}^{P} &= \pm\left(\frac{c_{P_0}G}{2\pi}\right) \\ &\quad\times\sqrt{\left[-\frac{a_{11}+a_{22}}{2} + \sqrt{\frac{(a_{11}+a_{22})^2}{4} - a_{11}a_{22} + a_{12}a_{21}}\right]}, \\ v_{ph}^{S} &= \pm\left(\frac{c_{P_0}G}{2\pi}\right) \\ &\quad\times\sqrt{\left[-\frac{a_{11}+a_{22}}{2} - \sqrt{\frac{(a_{11}+a_{22})^2}{4} - a_{11}a_{22} + a_{12}a_{21}}\right]}, \end{aligned} \tag{10}$$

where v_{ph}^{P} corresponds to the P-wave mode and v_{ph}^{S} corresponds to the S-wave mode.

For $\epsilon < \delta$, the term beneath the outer square root is negative for v_{ph}^{S}, which implies that the S-wave will grow exponentially during modeling, leading to numerical instabilities. This is consistent with the analytical plane-wave analysis of the VTI acoustic wave equation of Alkhalifah (2000), which shows that one set of complex-conjugate solutions is unstable when $\epsilon < \delta$ (Alkhalifah, 2000; solution a2 in his Figure 1). The instability of the S-wave mode is also shown by the expression of the S-wave phase velocity, which becomes imaginary when $\epsilon < \delta$ and $V_{S_0} = 0$ (Grechka et al., 2004; their equations 1 and 5).

In spite of the intrinsic instability of the S-wave mode, we see later that we can perform stable numerical simulations of the P-wave mode when $\epsilon < \delta$ using our frequency-domain method. In fact, we show that no S-waves are excited during frequency-domain simulation when $\epsilon < \delta$. We suggest that the excitation of the unstable S-wave mode is cancelled out by the absorbing boundary conditions implemented in the frequency-domain boundary value problem.

Table 1. Optimal weighting coefficients for the anisotropic mixed-grid stencil.

w_{m1}	w_{m2}	w_1
0.6291844	0.3708126	0.4258673

We apply the same dispersion analysis to the mixed-grid stencil. To estimate the weighting coefficients w_1, w_{m1}, and w_{m3}, we define the following cost function:

$$C(w_1, w_{m1}, w_{m2}) = \sum_{\phi}\sum_{G}\sum_{\delta}\sum_{\epsilon}[f(G,\phi,\delta,\epsilon,\theta)]^2, \tag{11}$$

with the function f defined as $f(G,\phi,\delta,\epsilon,\theta) = 1 - \tilde{v}_{ph}^{P}$. Here, $\tilde{v}_{ph}^{P}$ is the numerical phase velocity normalized by the exact P-wave velocity for VTI media. The exact P- and S-wave velocities for VTI media are given in Tsvankin (2001; his equation 1.55).

We minimize the cost function by considering simultaneously four values of G (0.1, 0.15, 0.2, and 0.25), four representative values of the (δ,ϵ) pairs taken from Thomsen (1986) [(0.148 0.091), (−0.012 0.137), (0.057 0.081), and (0.1 0.225)], $\theta = 0$, and six values of ϕ ranging from 0° to 75°. The cost function is minimized with a very fast simulated annealing algorithm (Sen and Stoffa, 1995). We obtain the coefficients $w_{m1} = 0.6291844$, $w_{m2} = 0.3708126$, and $w_1 = 0.4258673$ for a final rms of 1.4947164E-04 (Table 1).

The normalized phase-velocity dispersion curves for the two modes are shown in Figure 2 for ϕ ranging from 0° to 75° and for $\delta = 0.1$ and $\epsilon = 0.2$. These curves can be compared with those obtained with the RS and CS stencils, respectively, to determine the accuracy improvement provided by the mixed-grid and antilumped mass strategies (see Operto et al., 2007a; their Figure 2a and b).

The dispersion curves for the P-mode shown in Figure 2a suggest that four grid points per wavelengths will provide sufficiently accurate simulations of P-waves in homogeneous media. Indeed, the maximum phase-velocity error is 0.4% for $G = 4$, whereas the average error is on the order of 0.1% the value of $\mathbf{I}$ (Figure 2a). The phase-velocity dispersion curves of the second mode normalized by the exact phase velocity of the SV-wave confirm that the second mode of the TTI acoustic equation corresponds to an S-wave. This curve is not shown for $\phi = 0$ because the phase velocity of the S-wave is nil on the symmetry axis, through construction of the acoustic equation of Alkhalifah (2000). We verified during dispersion analysis that this velocity remains nil after discretization.

SOURCE EXCITATION

It is well acknowledged that applying a pressure source in the acoustic VTI/TTI equation leads to exciting an S-wave with a characteristic diamond shape (Alkhalifah, 2000; Grechka et al., 2004; Zhang et al., 2005).

Anderson et al. (2008) propose to modify the pressure source to cancel the shear strains and therefore the excitation of the S-waves in acoustic anisotropic media. The moment tensor source equivalent to a pressure source can be written as

$$\begin{aligned} \frac{dM_{11}}{dt} &= -s_1 P, \\ \frac{dM_{33}}{dt} &= -s_3 P. \end{aligned} \tag{12}$$

For an isotropic source, the weighting coefficients s_1 and s_3 equal one. In anisotropic acoustic media, we use $s_1 = 2((C_{11} + C_{13})/(C_{11} + C_{13} + C_{13} + C_{33}))$ and $s_3 = 2((C_{13} + C_{33})/(C_{11} + C_{13} + C_{13} + C_{33}))$, where the C_{ij} coefficients denote the elastic moduli.

We first apply the isotropic and anisotropic moment tensor sources to the 2D VTI elastodynamic system for which the S-wave velocity on the symmetry axis is set to zero (this gives $C_{44} = 0$) to mimic acoustic propagation (Anderson et al., 2008):

$$\begin{cases} \dfrac{\partial v_x}{\partial t} = b\dfrac{\partial \tau_{xx}}{\partial x} \\ \dfrac{\partial v_z}{\partial t} = b\dfrac{\partial \tau_{zz}}{\partial z} \\ \dfrac{\partial \tau_{xx}}{\partial t} = C_{11}\dfrac{\partial v_x}{\partial x} + C_{13}\dfrac{\partial v_z}{\partial z} \\ \dfrac{\partial \tau_{zz}}{\partial t} = C_{13}\dfrac{\partial v_x}{\partial x} + C_{33}\dfrac{\partial v_z}{\partial z} \end{cases}. \tag{13}$$

Note that equation 13 is not equivalent to the acoustic equation considered in our study. The anisotropic moment tensor source can be implemented in equation 13 by incrementing at each time step the normal stresses τ_{xx} and τ_{zz} by $-s_1P$ and $-s_3P$, respectively (Coutant et al., 1995).

We discretize equation 13 in the time domain using the RS stencil (Saenger et al., 2000). The source wavelet is a Ricker wavelet with a 4-Hz dominant frequency. The P-wave velocity on the symmetry axis is 2 km/s, $\delta = 0.1$, and $\epsilon = 0.2$. The grid interval is 10 m. The RS stencil requires that the spatial distribution of the point source with a 2D Gaussian function is spread to guarantee an effective coupling between the stress and the particle velocity staggered grids (Hustedt et al., 2004). Here, we use horizontal and vertical correlation lengths of 40 m.

Snapshots for the isotropic ($s_1 = s_3 = 1$) and anisotropic ($s_1 = 2((C_{11} + C_{13})/(C_{11} + C_{13} + C_{13} + C_{33}))$ and $s_3 = 2((C_{13} + C_{33})/(C_{11} + C_{13} + C_{13} + C_{33}))$ moment tensor sources are shown in Figure 3a and b. Use of the anisotropic source helps to attenuate the S-wave efficiently. However, the spatial smoothing of the point source is a second feature required to attenuate the S-wave. Indeed, the S-wave has a higher wavenumber content than the P-wave (see Bale, 2007; his Figure 1a). Therefore, a spatial smoothing of the source can be found such that it partially low-pass filters the S-wave without affecting the P-wavefront.

We also performed a simulation with the CS stencil that does not require smoothing the source (Hustedt et al., 2004). Without smoothing the point source, the attenuation of the S-wave was much less efficient than in Figure 3b. This is not a result of the stencil geometry because we verified that the CS and the RS stencils led to the same S-wave attenuation when the source was smoothed in the same manner.

In a second step, we applied the isotropic and anisotropic moment tensor sources to the acoustic VTI equation, recast as a first-order hyperbolic system (equation 3) in the time domain (Figure 3c and d). The RS stencil was used to discretize equation 3. The pressure source was implemented with horizontal and vertical dipoles applied to the third and fourth equations of expression 3. Each dipole was weighted by coefficients s_1 and s_2. The source was smoothed with a 2D Gaussian function; horizontal and vertical correlation lengths were 40 m. Although the S-wave was weakened, it was not fully canceled when the anisotropic moment tensor source was used (Figure 3d). To remove the S-wave efficiently, a correlation length as great as 80 m must be used, which leads to significant attenuation and distortion of the P-wavefront (Figure 3e and f).

So far, we have failed to remove the S-wave excitation efficiently at the source in the case of the acoustic anisotropic equation when the source is located in a medium with $\delta < \epsilon$. To avoid exciting the S-wave, the source can be set in an isotropic layer or in an elliptically anisotropic layer.

PML ABSORBING BOUNDARY CONDITION

PML absorbing boundary conditions provided a good absorption of the waves on the edges of the model. However, we have observed instabilities in the PML layers in the TTI case (i.e., when the symmetry axis is tilted with respect to the vertical and horizontal PML-PML interfaces). These instabilities, which are seen only when the number of grid points per wavelength is significantly greater than four and when $\epsilon > \delta$, are likely caused by the S-waves. When the grid interval is set according to the rule of four grid points per P-wavelength, the S-waves are affected strongly by numerical dispersion, which may cancel out the instability (Hu, 2001). When $\epsilon < \delta$, no S-waves are excited during frequency-domain modeling and no instability is seen, whatever the discretization.

The instability of PMLs in anisotropic media is studied theoretically by Bécache et al. (2003). They show in their Figure 13 that a necessary condition to guarantee the stability of PMLs is that, along the velocity curves, the slowness vector and the group velocity are oriented in the same way with respect to the Cartesian axis (i.e., the PML-PML interfaces). We plot the velocity curves for the S-waves in a homogeneous medium for a vertical symmetry axis and for a 45° rotated axes (Figure 4). When the symmetry axis is tilted, the group velocity vector and the slowness vector do not satisfy the geometric stability criterion of Bécache et al. (2003) (Figure 4b), contrary to the case where the symmetry axis is vertical (Figure 4a). Further study is required to remove this instability.

NUMERICAL EXAMPLES

In this section, we validate our method against analytical solutions along the symmetry axis and numerical solutions computed in 2D VTI elastic media with a classic staggered-grid velocity-stress FDTD method.

Simulation in homogeneous media

We first validate the method against an analytical solution along the symmetry axis available for class IV TI media (Payton, 1983).

Strong anisotropy: Zinc crystal

For the simulation, we consider a zinc crystal (Carcione et al., 1988; Komatitsch et al., 2000); properties are summarized in Table 2. The model measures 3300 × 3300 m with grid intervals for the acoustic FDFD and elastic FDTD simulations of 15 and 5 m, respectively. The source is in the middle of the grid. The source wavelet is a Ricker wavelt with a dominant frequency of 17 Hz. A horizontal receiver line is located above the source at a distance of 1 km. The symmetry axis is vertical.

Snapshots computed with the acoustic FDFD and elastic FDTD methods are shown in Figure 5. The analytical velocity and wavefront contours for the quasilongitudinal and quasitransverse modes are superimposed in both snapshots (Carcione et al., 1988). Good kinematic agreement is obtained between the analytical P- and S-velocity curves and the VTI elastic wavefronts (Figure 5b), whereas some mismatch is seen between the qP-wave analytical velocity curve and the VTI acoustic wavefront for directions of propagation midway between the symmetry axis and its perpendicular. Comparisons between the two snapshots of Figure 5 also suggest strongly overestimated amplitudes in the acoustic solution perpendicular to the symmetry axis.

Time-domain synthetic seismograms computed with the acoustic FDFD and elastic FDTD methods are compared in Figures 6 and 7. Good kinematic and dynamic agreement between the two solutions is obtained only for propagation directions close to the symmetry axis. This is further confirmed by a comparison of analytical seismograms and VTI acoustic seismograms recorded along the symmetry axis, which shows good agreement (Figure 7).

For the zinc crystal, $\epsilon = 0.83$ is significantly smaller than $\delta = 2.7$ (Table 2). This set of Thomsen's parameters should lead to unstablesimulation of the S-waves with the VTI acoustic equation. In contrast, we did not see any excitation of S-waves in our frequency-domain simulation when $\epsilon < \delta$ (Figure 5), and simulation of the

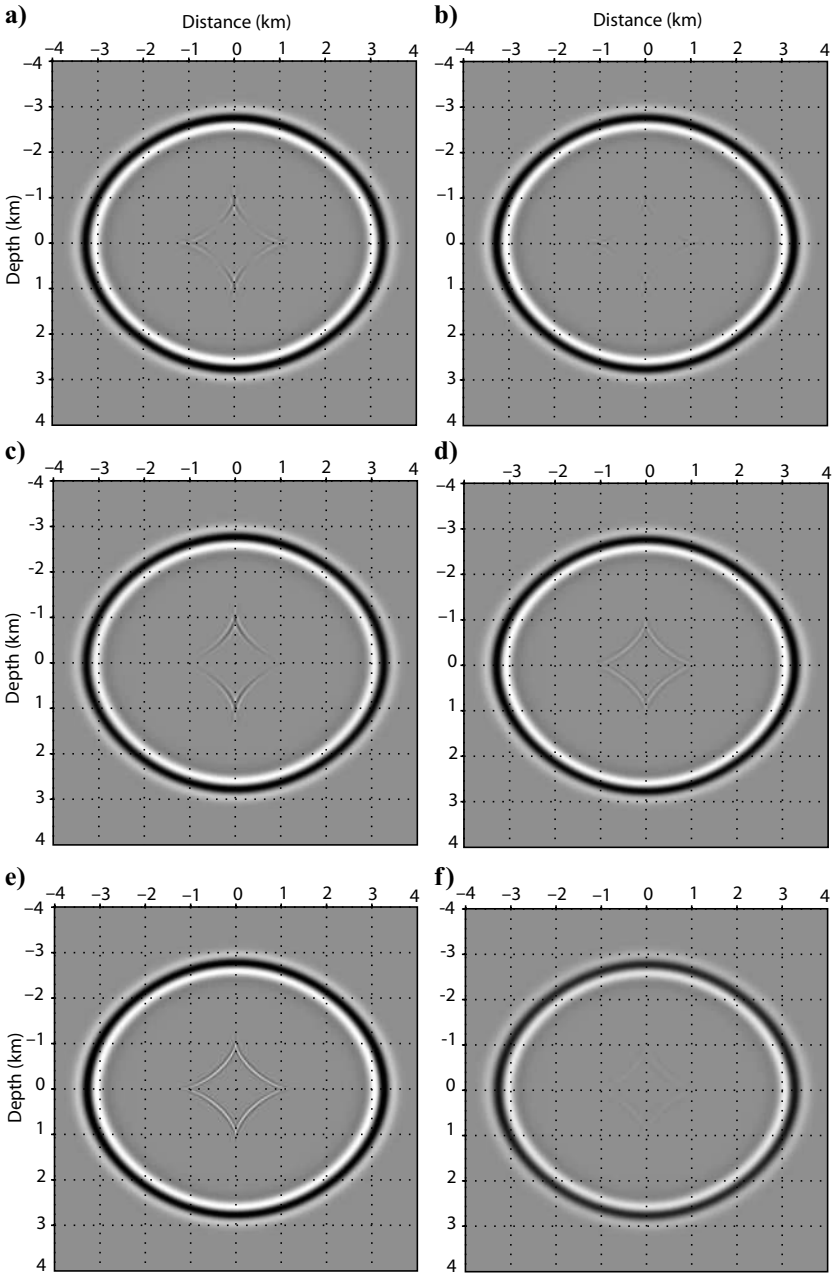

Figure 3. Source implementation. (a) Simulation using the RS staggered-grid stencil and an isotropic pressure source. The wave equation is the elastodynamic system within which the S-wave velocity on the symmetry axis is set to zero (equation 13). (b) As for (a), except an anisotropic pressure source is used (see text for details). (c) As for (a), except the acoustic anisotropic equation considered in this study is used for the simulation; an isotropic pressure source is used. (d) As for (c), except an anisotropic pressure source is used; note the less efficient attenuation of the S-wave than in (b). (e–f) As for (c), except the horizontal and vertical correlation lengths of the Gaussian function used to smooth the point source are (e) 20 and (g) 80 m.

P-waves remained stable. A possible reason is that the absorbing conditions implemented in the boundary-value frequency-domain problem cancel out this unstable mode. The ability to perform stable frequency-domain simulation of P-waves without exciting undesired S-waves when $\epsilon < \delta$ is confirmed in the following section.

This numerical example confirms that the acoustic approximation of wave propagation in VTI media does not lead to accurate solutions in cases of strong anisotropy. However, a comparison between numerical and analytical solutions along the symmetry axis provides the first validation of the implementation of the VTI acoustic mixed-grid stencil.

Weak anisotropy: Sediment

We repeat the numerical experiment on a material involving weaker anisotropy with the medium properties summarized in Table 2, for this example, $\epsilon > \delta$. The grid dimensions, the source wavelet, and the acquisition system are the same as in the previous case. The symmetry axis is vertical.

Snapshots computed with the acoustic FDFD and the elastic FDTD methods are compared in Figure 8a. The diamond-shaped S-wave is seen in the acoustic snapshot because $\epsilon > \delta$. Good kinematic agreement is now seen between the acoustic snapshot and the P-wavefront curve, whatever the direction of propagation. Acoustic FDFD and elastic FDTD seismograms show good agreement from kinematic and dynamic viewpoints (Figure 8b). This numerical example shows that the acoustic approximation of VTI wave propagation provides accurate simulation in homogeneous media in weak to moderate anisotropy.

We next consider the same simulation but for a 45° tilted symmetry axis. A snapshot computed with the acoustic FDFD method is shown in Figure 9a. The receiver line is rotated by 45° to compare the TTI acoustic seismograms with the VTI elastic ones computed with the FDTD method. Good agreement is obtained between TTI acoustic seismograms and VTI elastic seismograms (Figure 9b). The PMLs cause strong instabilities because the grid interval cannot be matched to each frequency when computing time-domain seismograms from a frequency-domain algorithm (Figure 9a). For this simulation, the PML instability is mitigated by the C-PML functions and complex-valued frequencies, used to remove wraparound (Mallick and Frazer, 1987).

Simulation in anticline medium

We now consider a heterogeneous medium composed of two layers delineated by a bell-shaped interface (Figure 10a). The properties of the two media are summarized in Table 3. The upper layer is homogeneous, whereas the P-wave velocity increases linearly with depth in the bottom layer to generate turning waves of significant amplitudes at long offset. The velocity gradient for the P-wave velocity in the bottom layer is 0.2 s^{-1}. The other parameters are constant in the bottom layer.

This example is designed to test the accuracy of the numerical scheme when the dip of the structures varies with respect to the symmetry axis, which is vertical in this simulation. We set

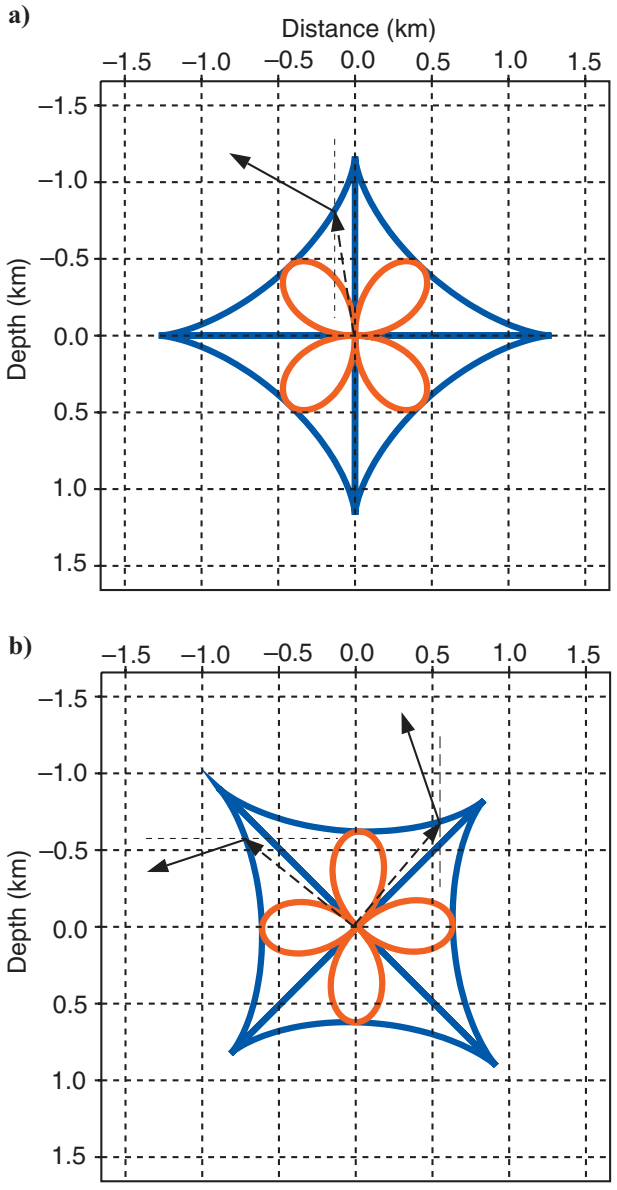

Figure 4. Geometric interpretation of the PML instability. Phase (red) and group (blue) velocity curves of the S-wave for the (a) VTI and (b) TTI cases. In (b), the tilt angle is 45°. The dashed arrows are along the velocity group vector; the solid arrows are along the slowness vectors, which are perpendicular to the wavefront. For the VTI case, both vectors have the same orientation with respect to the Cartesian axis (PML-PML interfaces); for the TTI case, they point in opposite directions.

Table 2. Properties of the zinc and sedimentary media for validation in homogeneous media.

Medium	V_P (m/s)	V_S (m/s)	ρ (kg/m^3)	δ	ϵ	θ (°)
Zinc	2955.06	2361	7100	2.70968	0.830645	0
Sediments	4000	2309	2500	0.02	0.1	0

$\epsilon < \delta$ in the upper medium, where the source is located, to avoid exciting the undesired S-waves at the source. The S-wave velocity used for the VTI elastic simulation is constant in the whole model and is equal to 2.361 km/s. The explosive source is a Ricker wavelt with a dominant frequency of 17 Hz. The model dimensions are 16,000 $\times$ 5000 m, and the grid intervals are 10 and 4 m for the VTI acousticFDFD and elastic FDTD simulations, respectively. The source is at a distance of 3.5 km and a depth of 0.4 km. A line of 171 receivers positioned every 40 m is 100 m above the source.

An 11.7-Hz monochromatic wavefield computed with the acoustic FDFD method shows a spurious arrival transmitted below the anticline (i.e., where the dip of the bell-shaped interface is not along or perpendicular to the symmetry axis) and superimposed on the transmitted P-wavefield (Figure 10b). This event is not seen at the vertex of the source where the interface is perpendicular to the symmetry axis. The spurious event corresponds to the conversion from the P-mode to the S-mode in the lower medium. The amplitudes of these P-to-S converted waves increase with the contrast between δ and ϵ at the interface.

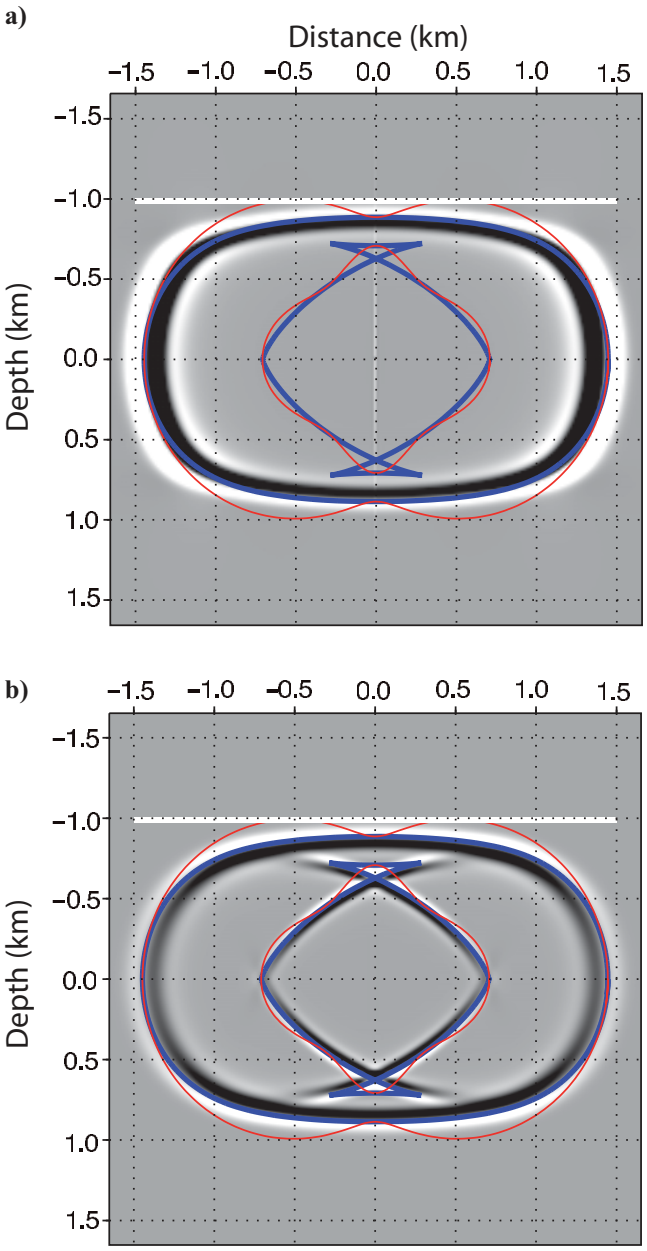

Figure 5. Modeling for the zinc model — VTI (a) elastic and (b) acoustic snapshots. The blue and red curves are the group and phase-velocity curves, respectively. The white line is the receiver line. The source is in the middle of the medium.

We repeat the simulation after smoothing the δ and ϵ models with a 2D Gaussian filter of horizontal and vertical correlation lengths of 60 m (Figure 10c). In this case, the P-to-S converted waves are removed (compare Figure 10b and c). We also verify that no P-to-S conversion occurs when ϵ is lower than δ in the two layers of the model. The VTI acoustic and elastic seismograms computed in the model of Figure 10a are compared in Figure 11. The acoustic seismograms are computed in the models without smoothing the δ and ϵ models. Reasonable agreement is obtained between the two sets of seismograms, although there is some mismatch between the amplitude-versus-offset behavior of the first arrival (illustrated by the variation of the polarity of the residual seismograms with offset in Figure 11c).

To reveal the arrivals generated by the P-to-S conversion at interfaces more clearly, we performed a simulation in a model composed of two homogeneous half-spaces separated by a dipping interface (Figure 12). The dip of the interface is 30°, whereas the symmetry axis is vertical. The properties of the two half-spaces are given in Table 3. A 17-Hz monochromatic wavefields for the p- and q-wavefield (Figure 12a and b) as well as a time-domain snapshot (Figure 12c) show that the dominant spurious event is an interface wave, labeled I in Figure 12c, that propagates along the interface with the P-wave velocity of the upper medium in the direction of the interface. This is first shown by the continuity between the direct P-wavefront in the upper medium and the head wavefront at the interface (Figure 12c).

The event is further confirmed by the seismograms of Figure 12d, recorded by a line of receivers 500 m below the interface. The slope of arrival I corresponds to the P-wave velocity in the upper medium for an incidence angle along the interface. We also observe the head wave labeled I′, which also propagates along the interface with the P-wave velocity of the lower medium in the direction of the interface.

The transmitted S-wavefront is rather difficult to interpret in Figure 12c. Interestingly, we performed one other simulation, where the interface was horizontal and the symmetry axis was vertical (Figure 13). In this case, the q-wavefield shows an evanescent wavefront propagating along the interface, and no interface waves propagate in the lower layer.

Simulation in the 2D anisotropic overthrust model

We now consider the simulation in a 2D section of the anisotropic overthrust model (Figure 14). The symmetry axis is vertical. The model dimensions are 20 $\times$ 4.4 km. The Thomsen's parameters δ and ϵ range between -0.176602 and 0.06 and between 0 and 0.2, respectively. The model embeds isotropic, elliptic anisotropic, and VTI layers. For the VTI elastic simulation, we consider a homogeneous S-wave velocity of 1.3 km/s to minimize the footprint of the S-waves. The explosive source is a Ricker wavelet of 6-Hz dominant frequency. The source is at a distance of 4 km and depth of 0.4 km with a line of 501 receivers spaced at 40-m intervals at 100 m depth. The grid interval for the acoustic simulation is 20 m, providing a fi-

nite-difference grid measuring 301×1081, including 800-m-thick PMLs along the four edges of the model. The grid interval for the elastic simulation is 10 m.

Acoustic and elastic snapshots can be compared in Figure 15. The footprint of the converted S-waves described in the previous section is seen clearly in the VTI layers of the acoustic snapshots. These events did not affect the acoustic seismograms recorded in the vicinity of the surface where the medium is isotropic because these S-waves remain confined to the VTI layers. The acoustic and the elastic seismograms compare well in Figure 16.

We now compare the computational efficiency of the FDFD and the FDTD approaches to compute monochromatic wavefields for multiple sources. These monochromatic wavefields typically represent the amount of data processed during one inversion iteration of single-frequency, frequency-domain FWI (Sirgue and Pratt, 2004; Brenders and Pratt, 2007a). In FDTD modeling, monochromatic wavefields can be computed by discrete Fourier transform in the loop over time steps (Sirgue et al., 2008).

The FDFD simulation in the overthrust model was performed using two nodes of a PC cluster, each node comprising two dual-core 2.4-GHz processors, providing 19.2 Gflops of peak performance per node. Each node had 8 Gb of RAM. The interconnection network between processors was Infiniband 4X. We used the massively parallel MUMPS direct solver to perform LU factorization and the for-

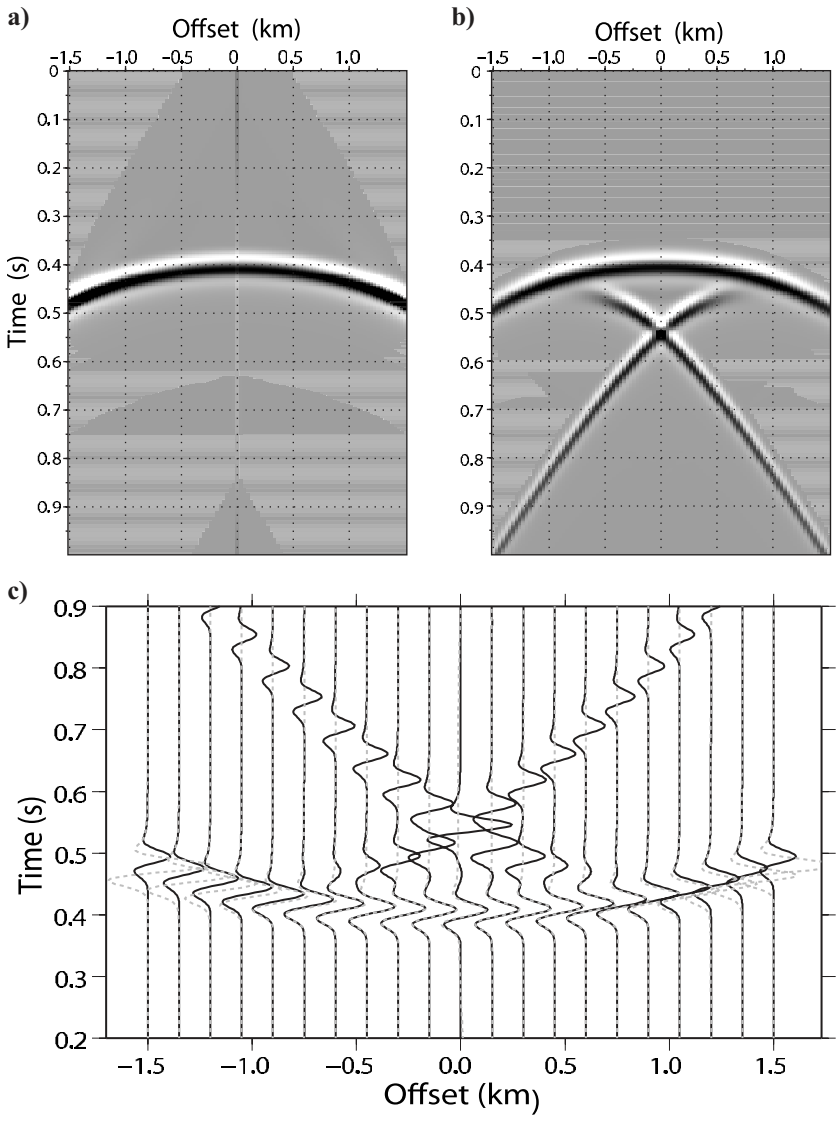

Figure 6. Modeling for the zinc model. (a) Acoustic seismograms. (b) Elastic seismograms. (c) Direct comparison between the acoustic (dashed gray) and elastic (solid black line) seismograms.

ward/backward substitutions in the FDFD modeling (Amestoy et al., 2006; Sourbier et al., 2009a, 2009b). The elapsed time for one parallel factorization was 68 s. The elapsed time to compute solutions for 64 sources by forward/backward substitutions was 8 s, leading to an elapsed time of 0.125 s per source. For elliptic anisotropy, the elapsed times for the factorization and for the 64 forward/backward substitutions decreased considerably to 3.5 s and 2 s, respectively, because the number of unknowns in the system decreased by a factor of two (the q-wavefield is nil).

The sequential elastic FDTD simulations took 1606 and 173 s for grid intervals of 10 and 20 m, respectively. The duration of the seismograms was 6 s. A grid interval of 10 m corresponds to the discretization required by an elastic FDTD simulation involving minimum S-wave velocities of 1 km/s and a maximum frequency of 20 Hz for an $\mathcal{O}(\Delta x^4)$ accurate stencil. A grid interval of 20 m was used for the FDFD simulation, corresponding to the discretization required by an acoustic simulation for a maximum frequency of 20 Hz.

Considering a coarse-grained parallelism over shots for FDTD simulation (which has an efficiency of one), the elapsed times to perform the modeling for the 64 shots distributed over the 8 MPI processes would be $1606 \times 64/8 = 12{,}848$ s and $173 \times 64/8 = 1384$ s for the 10- and 20-m grid intervals, respectively. The elapsed time of the acoustic and elastic FDTD simulations are significantly greater than the elapsed time of the acoustic FDFD simulation, i.e., $68 + 8 = 76$ s. These differences would increase dramatically with the number of sources. Thus, this numerical experiment confirms the conclusions inferred from the theoretical complexities of 2D FDFD and FDTD modeling (see Nihei and Li (2007) for a review) concerning the superiority of the frequency domain to compute monochromatic wavefields for many sources.

DISCUSSION

Two features of the modeling method presented in this study are the frequency-domain formulation and the acoustic approximation

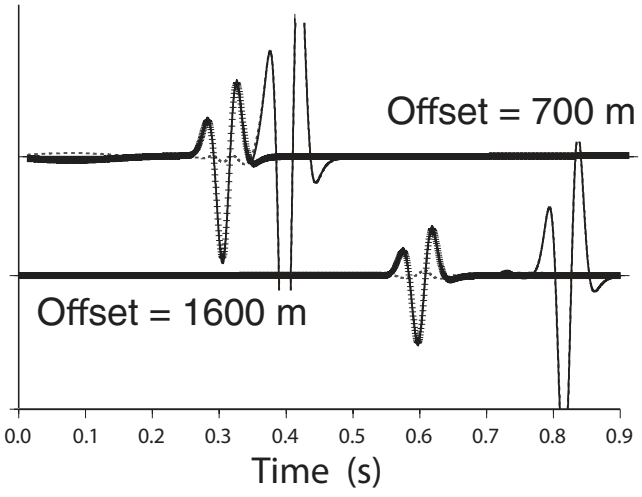

Figure 7. Modeling for the zinc model, comparing the analytical (solid line) and numerical acoustic seismograms on the symmetry axis for two offsets (700 and 1600 m). The difference is plotted with the dashed lines.

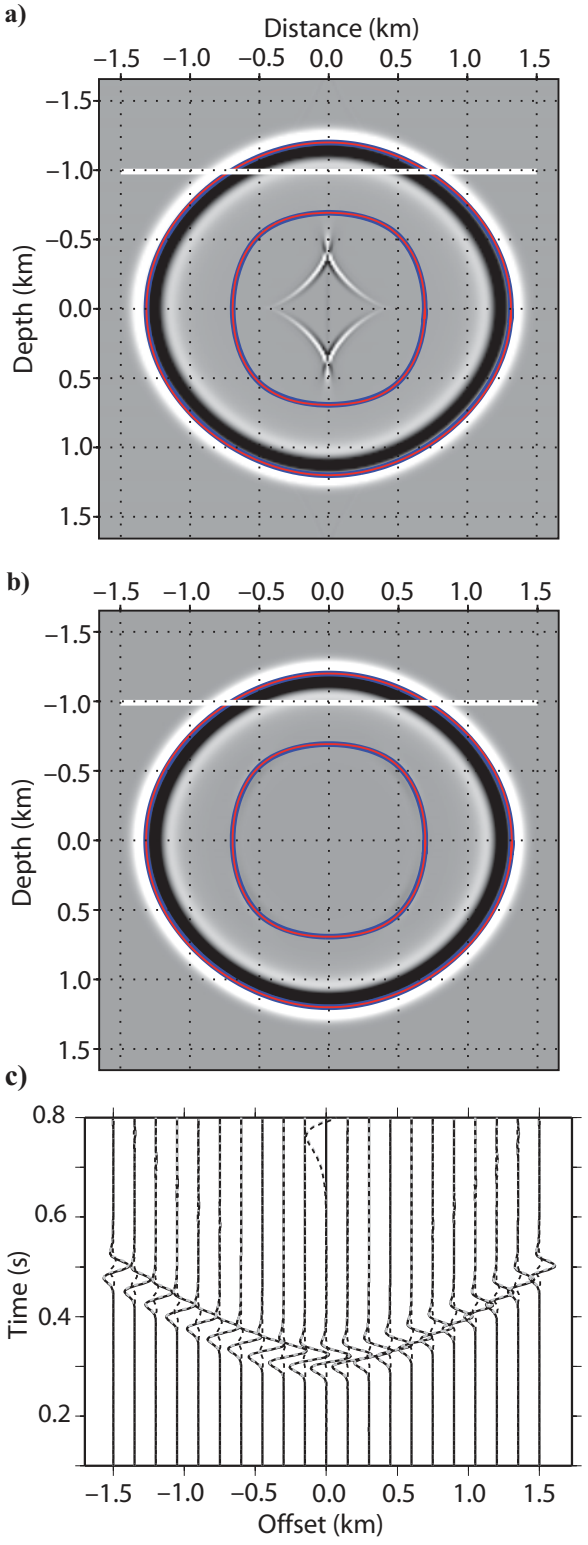

Figure 8. Modeling for the homogeneous sediment model — VTI (a) acoustic and (b) elastic snapshots. Time is 0.3 s. Velocity (blue) and wavefront (red) curves for the P- and S-modes are superimposed. (c) Direct comparison between acoustic (dashed gray line) and elastic (solid black line) seismograms. Difference is plotted with dashed black seismograms. The strong residual at 0 km offset and 0.6–0.8 s traveltimes is the result of the S-wave in the acoustic solution.

to model seismic wavefields in anisotropic media. Our main motivation behind the frequency domain and the acoustic approximation is to design a computationally efficient forward problem for imaging TTI media by frequency-domain FWI. Our numerical stencil provides sufficiently accurate solutions of the acoustic TTI wave equation when four grid points per wavelength are used for discretization. This discretization is suitable for FWI where the resolution limit is a half-wavelength.

Although the viscoacoustic TTI wave equation requires modeling two wavefields (the pressure wavefield plus the auxiliary wavefield q) as the elastic wave equation (two particle velocity wavefields), acoustic modeling remains significantly less demanding computationally than elastic modeling, mainly because the elastic wave equation is discretized according to the minimum S-wavelength. We also verify numerically the superior computational efficiency of the frequency-domain approach compared to time-domain approaches for multisource modeling of monochromatic wavefields.

Our second motivation behind the acoustic approximation is to mitigate the ill-posedness of FWI. Part of FWI ill-posedness results from partial coupling between different classes of parameters. A possible way to mitigate the ill-posedness is to consider simplifying assumptions in the physics of wave propagation — in other words, to limit the number of parameter classes in the medium parameterization. It is also worth noting that the footprint of anisotropy in P-waves is less complex than that affecting S-waves because P-waves are not split in two modes yet have a hyperbolic reflection moveout in anisotropic media (Tsvankin, 2001). The ill-posedness of the FWI also results from the sensitivity of local optimization approaches for inaccuracies of the starting model. This sensitivity increases in elastic FWI because S-waves have higher resolution power than P-waves as a result of their smaller wavelengths. The higher resolution power of S-waves requires more accurate S-wave-velocity starting models or a lower starting frequency to make the inversion converge toward acceptable velocity models (Brossier et al., 2008).

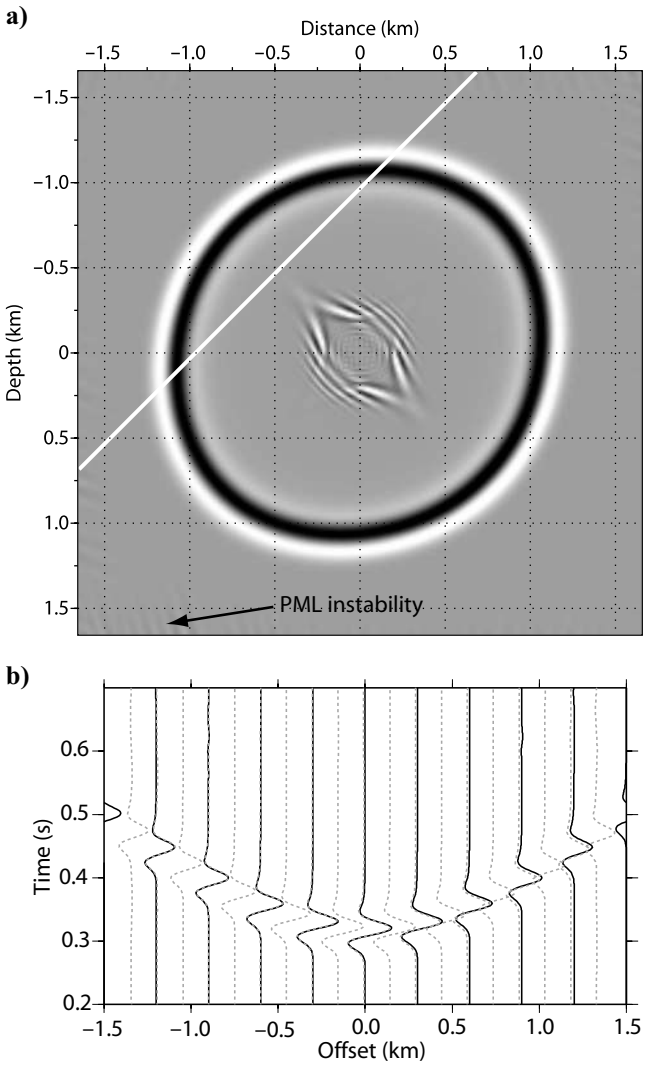

Figure 9. (a) Snapshot computed for the TTI acoustic homogeneous medium. The symmetry axis is rotated by 45° with respect to the vertical. The white line denotes the position of the receivers. The arrow points out spurious signals resulting from PML instability. (b) Direct comparison between the TTI acoustic (dashed gray line) and VTI elastic (solid black line) seismograms.

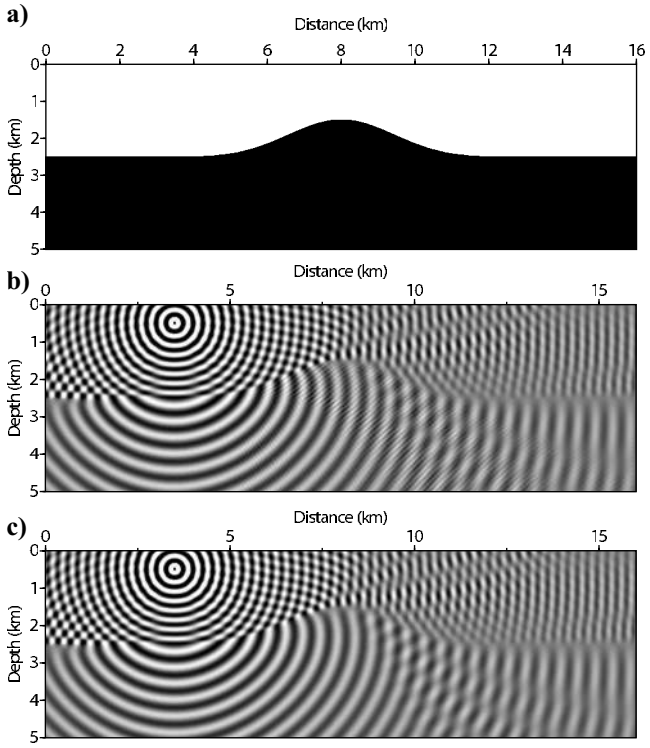

Figure 10. (a) Anticline model. (b) Monochromatic wavefield. Note the spurious event transmitted in the lower medium, where the dip of the interface is significant with respect to the symmetry axis. (c) As for (b), except the δ and ϵ models are smoothed with a 2D Gaussian filter of horizontal and vertical correlation lengths equal to six times the grid interval. Smoothing the contrast between the Thomsen parameters removes the artifact.

Indeed, the reliability of the acoustic anisotropic approximation in the framework of FWI can be questioned because acoustic media are intrinsically isotropic. The numerical experiments we present suggest that the viscoacoustic TTI wave equation is sufficiently accurate from a dynamic viewpoint for weak to moderate anisotropic media.

Regarding the footprint of the S-waves in viscoacoustic TTI modeling, the excitation of S-waves can be cancelled at the source by setting the source in an isotropic layer or in an elliptically anisotropic layer. Excitation of S-waves at the source can be cancelled out pragmatically by setting a small, smoothly tapered circular region with

Table 3. Properties of the anticline model. The P-wave velocity increases linearly with depth in the bottom layer with a gradient of 0.2 s^{-1}. The velocity on top of the layer is provided. The other parameters are constant.

Layer	V_P (m/s)	V_S (m/s)	ρ (kg/m^3)	δ	ϵ	θ (°)
Top	2955.06	2361.66	2200	0.143	− 0.035	0
Bottom	4820.73 (on top)	2361.66	2500	0.06	0.11	0

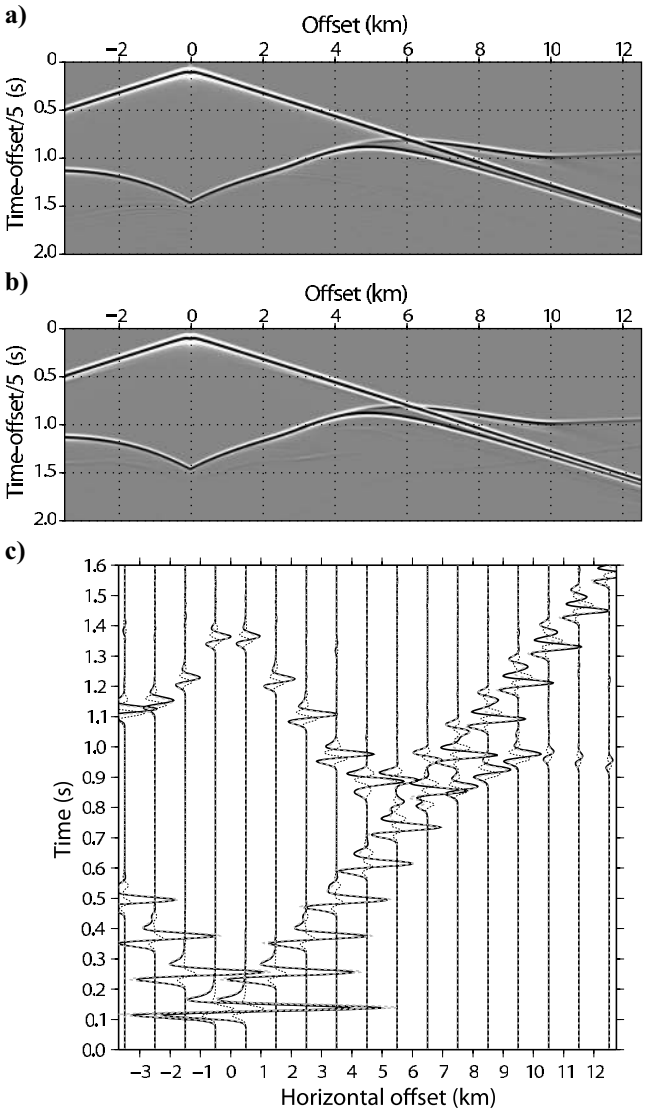

Figure 11. Anticline model simulation — (a) acoustic and (b) elastic seismograms. The seismograms are plotted with a reduction velocity of 5 km/s. Some artificial reflections are seen on the right end of the model in the case of the elastic simulation. (c) Direct comparison between acoustic (dashed gray line) and elastic (solid black line) seismograms. The differences are the thin dashed black line.

$\delta = \epsilon$ around the source (Duveneck et al., 2008). The P-to-S-mode-conversion at sharp interfaces cannot be removed efficiently without slightly smoothing the δ and ϵ contrasts, which is a last resort in FWI. However, our numerical experiments suggest that the P-to-S-mode converted waves do not affect reverse-time-migrated images significantly, possibly because of their small amplitudes (Duveneck et al., 2008).

A last issue concerns the extension to 3D modeling. The time and memory complexities of the direct solvers as well as their limited intrinsic scalability prevent large-scale modeling in 3D viscoacoustic TTI media with the approaches we develop (Operto et al., 2007b). Only elliptic anisotropy can be implemented in 3D FDFD approaches based on a direct solver because it does not introduce computational overhead compared to the isotropic case. For 3D large-scale applications, the acoustic VTI and TTI wave equations can be implemented easily in the time domain with explicit integration schemes (Duveneck et al., 2008; Fletcher et al., 2008; Lesage et al., 2008). The alternative FDFD approaches developed so far for the acoustic isotropic wave equation are based on hybrid direct/iterative solvers (Sourbier et al., 2008) or iterative solvers (Erlangga and Herrmann, 2008). These approaches also can be viewed for 3D viscoacoustic

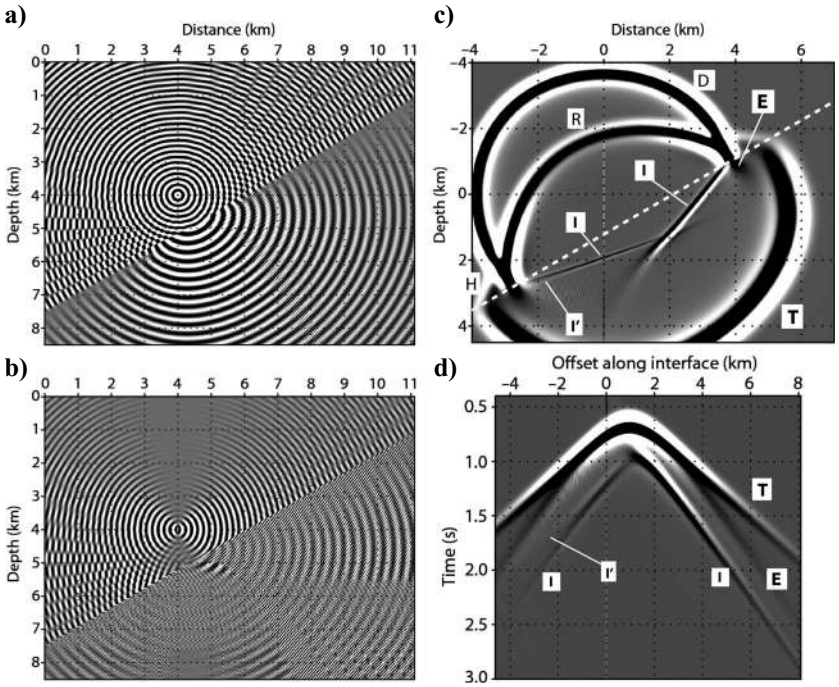

Figure 12. Monochromatic (a) p- and (b) q-wavefields in the dipping-layer model. (c) Time-domain snapshot. Nomenclature: D — direct P-wave; R — reflected P-wave; T — transmitted P-wave; H — P head wave; I and I′ — head waves ensuring the continuity between the transmitted P- and S-wavefronts I′ and between the reflected and transmitted S-wavefronts I; E — evanescent interface wave. (d) Time-domain seismograms recorded by a receiver line 500 m below the interface.

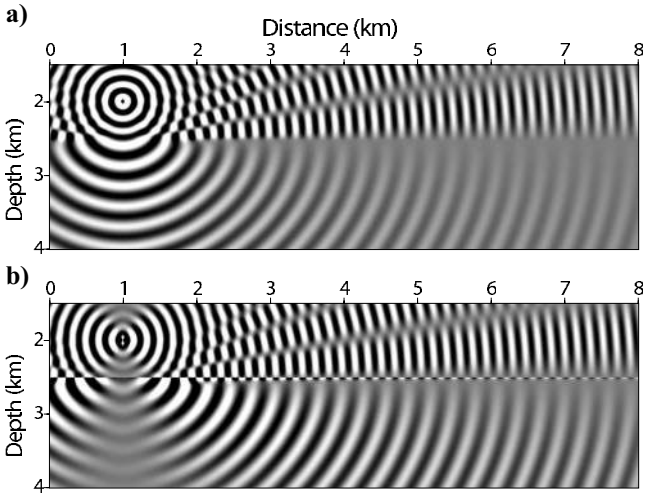

Figure 13. Monochromatic (a) p- and (b) q-wavefields in the case of two VTI half-spaces delineated by a flat interface. In this case, the interface wave is evanescent and does not lead to a conic wave in the lower medium.

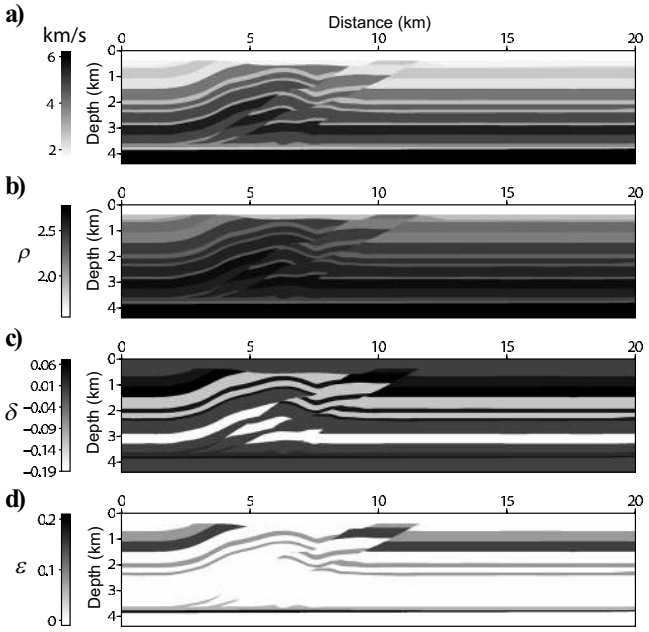

Figure 14. VTI overthrust model. (a) P-wave velocity; (b) density; (c) δ; (d) ϵ.

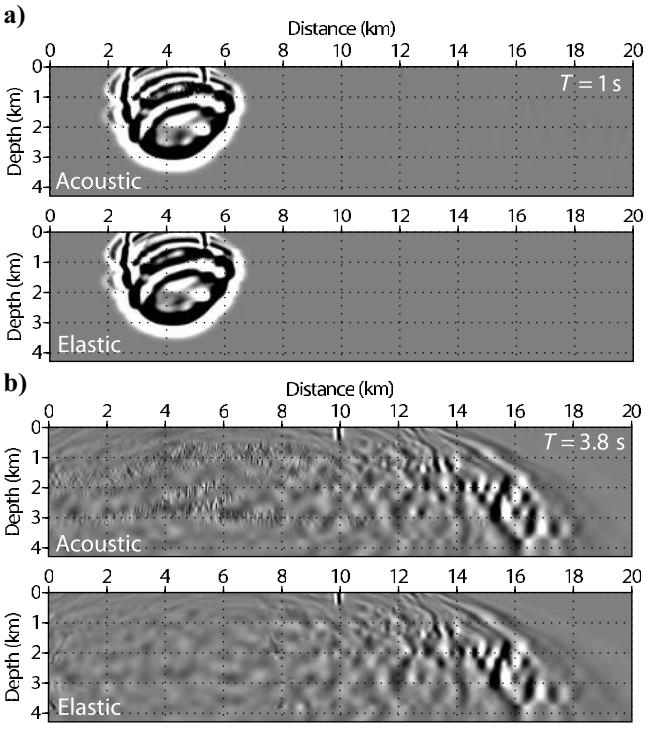

Figure 15. Simulation in the overthrust model. Acoustic (top panel) and elastic (bottom panel) snapshots for two propagation times: (a) 1 and (b) 3.8 s. The S-waves affect the acoustic wavefields in the VTI layers of the overthrust model.

TTI modeling in the future. Although the approaches we present in this study do not extend to 3D cases easily, efficient 2D algorithms remain useful in assessing the potential and limits of unconventional seismic imaging methods.

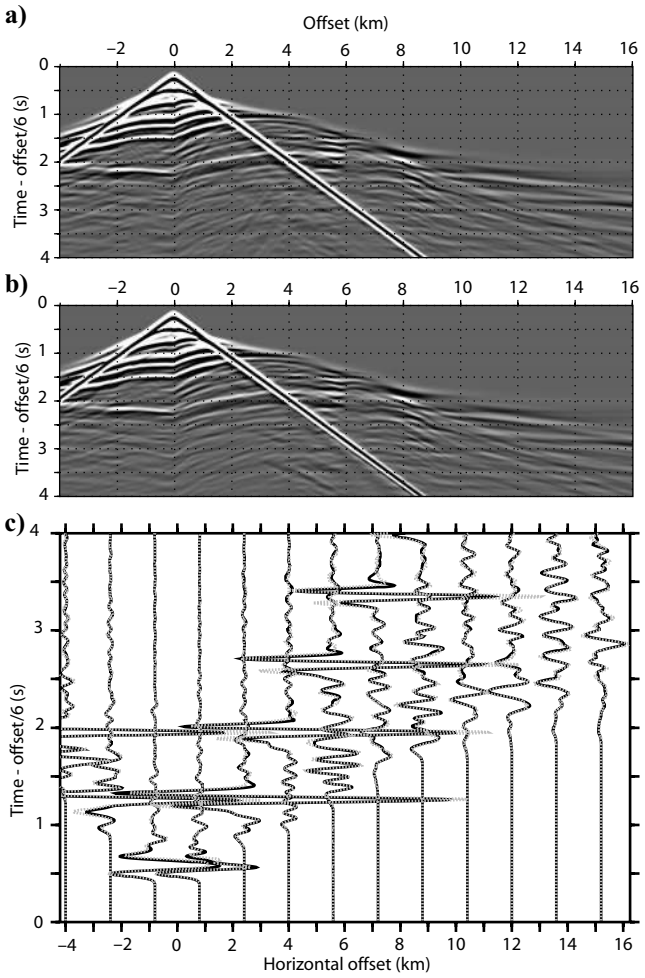

Figure 16. Synthetic seismograms computed in the overthrust model: (a) VTI acoustic seismograms; (b) VTI elastic seismograms; (c) direct comparison between acoustic (dashed gray line) and elastic (solid black line) seismograms. The seismograms are plotted with a reduction velocity of 6 km/s. The source is in an isotropic layer.

CONCLUSION

We have developed a computationally efficient FDFD method for multisource seismic wave modeling in 2D viscoacoustic TTI media. Comparisons between acoustic and elastic modeling in weak to moderate anisotropic media suggest that the method is sufficiently accurate for FWI from kinematic and dynamic viewpoints. The main limitation of the method is the propagation of S-waves in acoustic VTI and TTI media. Whereas S-wave excitation can be cancelled out pragmatically at the source, the P-to-S mode conversions occur at sharp contrasts between anisotropic parameters. The real footprint of these P-to-S converted waves must be assessed during the summation of the redundant information underlying full-waveform inversion. A last resort to avoid these mode conversions is to smooth the contrast between the anisotropic parameters δ and ϵ slightly. The S-wave mode is unstable in the acoustic anisotropic wave equation when $\epsilon < \delta$, but we observe that the S-waves are not excited during frequency-domain modeling in such media. Therefore, we performed stable simulations of the P-waves in the frequency domain unlike in the time domain. Future studies will involve interfacing the viscoacoustic TTI modeling method into a frequency-do-

main viscoacoustic full-waveform inversion code to assess the reliability of full-waveform inversion for imaging anisotropic parameters quantitatively.

ACKNOWLEDGMENTS

Access to the high-performance computing facilities of the Mesocentre SIGAMM computer center provided the required computer resources, and we gratefully acknowledge this facility and the support of its staff. This work was conducted within the framework of the SEISCOPE consortium, sponsored by BP, CGGVeritas, ExxonMobil, Shell, and TOTAL. This work was funded partly by the ANR project (ANR-05-NT05-2-42427). We thank Assistant Editor V. Grechka, Associate Editor M. van der Baan, E. Saenger, and two anonymous reviewers for their useful comments. We are especially grateful to V. Grechka for his useful comments on stability constraints in acoustic anisotropic media. We would like to thank W. A. Mulder (Shell International E&P BV) for providing us the anisotropic overthrust model (http://aniso.citg.tudelft.nl).

APPENDIX A

RS PARSIMONIOUS STAGGERED-GRID STENCIL

In this appendix, we provide the expression of the parsimonious RS staggered-grid stencil. The partial derivatives with respect to x and z can be replaced by a linear combination of the partial derivatives with respect to the rotated coordinates x' and z' in equation 5 (Figure 2):

$$\frac{\partial}{\partial x} = \frac{1}{\sqrt{2}}\left(\frac{\partial}{\partial x'} + \frac{\partial}{\partial z'}\right),$$
$$\frac{\partial}{\partial z} = \frac{1}{\sqrt{2}}\left(-\frac{\partial}{\partial x'} + \frac{\partial}{\partial z'}\right). \quad \text{(A-1)}$$

The first-order differential operators with respect to x' and z' are discretized with the following stencils:

$$\left[\frac{\partial g}{\partial x'}\right]_{ij} = \frac{1}{\sqrt{2}h}[g_{i+1/2,j-1/2} - g_{i-1/2,j+1/2}],$$
$$\left[\frac{\partial g}{\partial z'}\right]_{ij} = \frac{1}{\sqrt{2}h}[g_{i+1/2,j+1/2} - g_{i-1/2,j-1/2}]. \quad \text{(A-2)}$$

We first discretize the first two equations of system 5 using discrete scheme A-2. Then, we define the expression of wavefields p_x, q_x, p_z, and q_z at the grid positions required by the discrete form of the first two equations of system 5 using discrete scheme A-2. Finally, we inject the resulting expressions of p_x, q_x, p_z, and q_z into the first two equations to derive the second-order discrete equation in p and q.

Gathering the terms with respect to the indices of the p-wavefield gives nine coefficients of the RS stencil for the submatrix A_r of equation 6:

$$\begin{aligned}
A_{r_{ij}} = &-\frac{1}{4\xi_{x_i}h^2}A_{x_{ij}}\left(\frac{b_{i+1/2,j-1/2}}{\xi_{x_{i+1/2}}} + \frac{b_{i-1/2,j+1/2}}{\xi_{x_{i-1/2}}}\right.\\
&\left.+ \frac{b_{i+1/2,j+1/2}}{\xi_{x_{i+1/2}}} + \frac{b_{i-1/2,j-1/2}}{\xi_{x_{i-1/2}}}\right)\\
&+ \frac{1}{4\xi_{x_i}h^2}B_{x_{ij}}\left(\frac{b_{i+1/2,j-1/2}}{\xi_{z_{j-1/2}}} + \frac{b_{i-1/2,j+1/2}}{\xi_{z_{j+1/2}}}\right.\\
&\left.- \frac{b_{i+1/2,j+1/2}}{\xi_{z_{j+1/2}}} - \frac{b_{i-1/2,j-1/2}}{\xi_{z_{j-1/2}}}\right)\\
&+ \frac{1}{4\xi_{z_j}h^2}A_{z_{ij}}\left(\frac{b_{i+1/2,j-1/2}}{\xi_{x_{i+1/2}}} + \frac{b_{i-1/2,j+1/2}}{\xi_{x_{i-1/2}}}\right.\\
&\left.- \frac{b_{i+1/2,j+1/2}}{\xi_{x_{i+1/2}}} - \frac{b_{i-1/2,j-1/2}}{\xi_{x_{i-1/2}}}\right)\\
&- \frac{1}{4\xi_{z_j}h^2}B_{z_{ij}}\left(\frac{b_{i+1/2,j-1/2}}{\xi_{z_{j-1/2}}} + \frac{b_{i-1/2,j+1/2}}{\xi_{z_{j+1/2}}}\right.\\
&\left.+ \frac{b_{i+1/2,j+1/2}}{\xi_{z_{j+1/2}}} + \frac{b_{i-1/2,j-1/2}}{\xi_{z_{j-1/2}}}\right), \quad \text{(A-3)}
\end{aligned}$$

$$\begin{aligned}
A_{r_{i+1,j}} = &+ \frac{1}{4\xi_{x_i}h^2}A_{x_{ij}}\left(\frac{b_{i+1/2,j-1/2}}{\xi_{x_{i+1/2}}} + \frac{b_{i+1/2,j+1/2}}{\xi_{x_{i+1/2}}}\right)\\
&+ \frac{1}{4\xi_{x_i}h^2}B_{x_{ij}}\left(\frac{b_{i+1/2,j-1/2}}{\xi_{z_{j-1/2}}} - \frac{b_{i+1/2,j+1/2}}{\xi_{z_{j+1/2}}}\right)\\
&+ \frac{1}{4\xi_{z_j}h^2}A_{z_{ij}}\left(-\frac{b_{i+1/2,j-1/2}}{\xi_{x_{i+1/2}}} + \frac{b_{i+1/2,j+1/2}}{\xi_{x_{i+1/2}}}\right)\\
&+ \frac{1}{4\xi_{z_j}h^2}B_{z_{ij}}\left(-\frac{b_{i+1/2,j-1/2}}{\xi_{z_{j-1/2}}} - \frac{b_{i+1/2,j+1/2}}{\xi_{z_{j+1/2}}}\right), \quad \text{(A-4)}
\end{aligned}$$

$$\begin{aligned}
A_{r_{i-1,j}} = &\frac{1}{4\xi_{x_i}h^2}A_{x_{ij}}\left(\frac{b_{i-1/2,j+1/2}}{\xi_{x_{i-1/2}}} + \frac{b_{i-1/2,j-1/2}}{\xi_{x_{i-1/2}}}\right)\\
&+ \frac{1}{4\xi_{x_i}h^2}B_{x_{ij}}\left(\frac{b_{i-1/2,j+1/2}}{\xi_{z_{j+1/2}}} - \frac{b_{i-1/2,j-1/2}}{\xi_{z_{j-1/2}}}\right)\\
&+ \frac{1}{4\xi_{z_j}h^2}A_{z_{ij}}\left(-\frac{b_{i-1/2,j+1/2}}{\xi_{x_{i-1/2}}} + \frac{b_{i-1/2,j-1/2}}{\xi_{x_{i-1/2}}}\right)\\
&+ \frac{1}{4\xi_{z_j}h^2}B_{z_{ij}}\left(-\frac{b_{i-1/2,j+1/2}}{\xi_{z_{j+1/2}}} - \frac{b_{i-1/2,j-1/2}}{\xi_{z_{j-1/2}}}\right), \quad \text{(A-5)}
\end{aligned}$$

$$A_{r_{i,j+1}} = \frac{1}{4\xi_{x_i}h^2}A_{x_{ij}}\left(-\frac{b_{i-1/2,j+1/2}}{\xi_{x_{i-1/2}}} - \frac{b_{i+1/2,j+1/2}}{\xi_{x_{i+1/2}}}\right) + \frac{1}{4\xi_{x_i}h^2}B_{x_{ij}}\left(-\frac{b_{i-1/2,j+1/2}}{\xi_{z_{j+1/2}}} + \frac{b_{i+1/2,j+1/2}}{\xi_{z_{j+1/2}}}\right) + \frac{1}{4\xi_{z_j}h^2}A_{z_{ij}}\left(\frac{b_{i-1/2,j+1/2}}{\xi_{x_{i-1/2}}} - \frac{b_{i+1/2,j+1/2}}{\xi_{x_{i+1/2}}}\right) + \frac{1}{4\xi_{z_j}h^2}B_{z_{ij}}\left(\frac{b_{i-1/2,j+1/2}}{\xi_{z_{j+1/2}}} + \frac{b_{i+1/2,j+1/2}}{\xi_{z_{j+1/2}}}\right), \quad \text{(A-6)}$$

$$A_{r_{i,j-1}} = \frac{1}{4\xi_{x_i}h^2}A_{x_{ij}}\left(-\frac{b_{i+1/2,j-1/2}}{\xi_{x_{i+1/2}}} - \frac{b_{i-1/2,j-1/2}}{\xi_{x_{i-1/2}}}\right) + \frac{1}{4\xi_{x_i}h^2}B_{x_{ij}}\left(-\frac{b_{i+1/2,j-1/2}}{\xi_{z_{j-1/2}}} + \frac{b_{i-1/2,j-1/2}}{\xi_{z_{j-1/2}}}\right) + \frac{1}{4\xi_{z_j}h^2}A_{z_{ij}}\left(\frac{b_{i+1/2,j-1/2}}{\xi_{x_{i+1/2}}} - \frac{b_{i-1/2,j-1/2}}{\xi_{x_{i-1/2}}}\right) + \frac{1}{4\xi_{z_j}h^2}B_{z_{ij}}\left(\frac{b_{i+1/2,j-1/2}}{\xi_{z_{j-1/2}}} + \frac{b_{i-1/2,j-1/2}}{\xi_{z_{j-1/2}}}\right), \quad \text{(A-7)}$$

$$A_{r_{i+1,j-1}} = \frac{1}{4\xi_{x_i}h^2}\left(A_{x_{ij}}\frac{b_{i+1/2,j-1/2}}{\xi_{x_{i+1/2}}} - B_{x_{ij}}\frac{b_{i+1/2,j-1/2}}{\xi_{z_{j-1/2}}}\right) + \frac{1}{4\xi_{z_j}h^2}\left(-A_{z_{ij}}\frac{b_{i+1/2,j-1/2}}{\xi_{x_{i+1/2}}} + B_{z_{ij}}\frac{b_{i+1/2,j-1/2}}{\xi_{z_{j-1/2}}}\right), \quad \text{(A-8)}$$

$$A_{r_{i-1,j+1}} = \frac{1}{4\xi_{x_i}h^2}\left(A_{x_{ij}}\frac{b_{i-1/2,j+1/2}}{\xi_{x_{i-1/2}}} - B_{x_{ij}}\frac{b_{i-1/2,j+1/2}}{\xi_{z_{j+1/2}}}\right) + \frac{1}{4\xi_{z_j}h^2}\left(-A_{z_{ij}}\frac{b_{i-1/2,j+1/2}}{\xi_{x_{i-1/2}}} + B_{z_{ij}}\frac{b_{i-1/2,j+1/2}}{\xi_{z_{j+1/2}}}\right), \quad \text{(A-9)}$$

$$A_{r_{i-1,j-1}} = \frac{1}{4\xi_{x_i}h^2}\left(A_{x_{ij}}\frac{b_{i-1/2,j-1/2}}{\xi_{x_{i-1/2}}} + B_{x_{ij}}\frac{b_{i-1/2,j-1/2}}{\xi_{z_{j-1/2}}}\right) + \frac{1}{4\xi_{z_j}h^2}\left(A_{z_{ij}}\frac{b_{i-1/2,j-1/2}}{\xi_{x_{i-1/2}}} + B_{z_{ij}}\frac{b_{i-1/2,j-1/2}}{\xi_{z_{j-1/2}}}\right), \quad \text{(A-10)}$$

and

$$A_{r_{i+1,j+1}} = \frac{1}{4\xi_{x_i}h^2}\left(A_{x_{ij}}\frac{b_{i+1/2,j+1/2}}{\xi_{x_{i+1/2}}} + B_{x_{ij}}\frac{b_{i+1/2,j+1/2}}{\xi_{z_{j+1/2}}}\right) + \frac{1}{4\xi_{z_j}h^2}\left(A_{z_{ij}}\frac{b_{i+1/2,j+1/2}}{\xi_{x_{i+1/2}}} + B_{z_{ij}}\frac{b_{i+1/2,j+1/2}}{\xi_{z_{j+1/2}}}\right), \quad \text{(A-11)}$$

where (i,j) denote the indices of a point in the 2D finite-difference grid located on the diagonal of the submatrix A_r.

The coefficients of the submatrices $\mathbf{B_r}$, $\mathbf{C_r}$, $\mathbf{D_r}$ in system 6 can be inferred easily from those of submatrix $\mathbf{A_r}$ by substituting the coefficients $A_{r_{ij}}$:

- $-A_x$ by C_x, E_x, G_x for submatrices $\mathbf{B_r}$, $\mathbf{C_r}$, $\mathbf{D_r}$, respectively
- $-B_x$ by D_x, F_x, H_x for submatrices $\mathbf{B_r}$, $\mathbf{C_r}$, $\mathbf{D_r}$, respectively
- $-A_z$ by C_z, E_z, G_z for submatrices $\mathbf{B_r}$, $\mathbf{C_r}$, $\mathbf{D_r}$, respectively
- $-B_z$ by D_z, F_z, H_z for submatrices $\mathbf{B_r}$, $\mathbf{C_r}$, $\mathbf{D_r}$, respectively.

APPENDIX B

CS PARSIMONIOUS STAGGERED-GRID STENCIL

We now discretize system 5 with the following second-order accurate staggered-grid stencils:

$$\left[\frac{\partial g}{\partial x}\right]_{ij} = \frac{1}{h}[g_{i+1/2,j} - g_{i-1/2,j}],$$
$$\left[\frac{\partial g}{\partial z}\right]_{ij} = \frac{1}{h}[g_{i+1/2,j} - g_{i-1/2,j}]. \quad \text{(B-1)}$$

We apply the same parsimonious strategy as for the RS stencil (Appendix A). In the final expression of the discrete second-order wave equation, the values of the p- and q-wavefields are required at five positions on the reference grid along a cross stencil (dark gray squares, Figure 2b) as well on the middle of the four adjacent cells delineated by the cross stencil (dashed squares, Figure 2b). These four latter values are replaced by interpolated ones on the nine points defined by the four adjacent cells (gray squares, Figure 2b) using a bilinear interpolation:

$$p_{i\pm1/2,j\pm1/2} = \frac{1}{4}(p_{i,j} + p_{i\pm1,j} + p_{i,j\pm1} + p_{i\pm1,j\pm1}). \quad \text{(B-2)}$$

We end up with nine coefficients for matrix A_c:

$$A_{c_{i,j}} = \frac{\omega^2}{\kappa_{ij}} + \frac{1}{\xi_{x_i}h^2}A_{x_{ij}}\left(-\frac{b_{i+1/2,j}}{\xi_{x_{i+1/2}}} - \frac{b_{i-1/2,j}}{\xi_{x_{i-1/2}}}\right) + \frac{1}{\xi_{z_j}h^2}B_{z_{ij}}\left(-\frac{b_{i,j+1/2}}{\xi_{z_{j+1/2}}} - \frac{b_{i,j-1/2}}{\xi_{z_{j-1/2}}}\right),$$
$$A_{c_{i+1,j}} = \frac{1}{\xi_{x_i}h^2}A_{x_{ij}}\frac{b_{i+1/2,j}}{\xi_{x_{i+1/2}}} + \frac{1}{4\xi_{z_j}h^2}A_{z_{ij}}\left(\frac{b_{i,j+1/2}}{\xi_{x_i}} - \frac{b_{i,j-1/2}}{\xi_{x_i}}\right),$$

$$
\begin{aligned}
A_{c_{i-1,j}} &= \frac{1}{\xi_{x_i} h^2} A_{x_{ij}} \frac{b_{i-1/2,j}}{\xi_{x_{i-1/2}}} + \frac{1}{4\xi_{z_j} h^2} A_{z_{ij}} \left(-\frac{b_{i,j+1/2}}{\xi_{x_i}} + \frac{b_{i,j-1/2}}{\xi_{x_i}} \right), \\
A_{c_{i,j+1}} &= \frac{1}{4\xi_{x_i} h^2} B_{x_{ij}} \left(-\frac{b_{i-1/2,j}}{\xi_{z_j}} + \frac{b_{i+1/2,j}}{\xi_{z_j}} \right) + \frac{1}{\xi_{z_j} h^2} B_{z_{ij}} \frac{b_{i,j+1/2}}{\xi_{z_{j+1/2}}}, \\
A_{c_{i,j-1}} &= \frac{1}{4\xi_{x_i} h^2} B_{x_{ij}} \left(-\frac{b_{i+1/2,j}}{\xi_{z_j}} + \frac{b_{i-1/2,j}}{\xi_{z_j}} \right) + \frac{1}{\xi_{z_j} h^2} B_{z_{ij}} \frac{b_{i,j-1/2}}{\xi_{z_{j-1/2}}}, \\
A_{c_{i+1,j-1}} &= -\frac{1}{4\xi_{x_i} h^2} B_{x_{ij}} \frac{b_{i+1/2,j}}{\xi_{z_j}} - \frac{1}{4\xi_{z_j} h^2} A_{z_{ij}} \frac{b_{i,j-1/2}}{\xi_{x_i}}, \\
A_{c_{i-1,j+1}} &= -\frac{1}{4\xi_{x_i} h^2} B_{x_{ij}} \frac{b_{i-1/2,j}}{\xi_{z_j}} + \frac{1}{4\xi_{z_j} h^2} A_{z_{ij}} \frac{b_{i,j+1/2}}{\xi_{x_i}}, \\
A_{c_{i+1,j+1}} &= \frac{1}{4\xi_{x_i} h^2} B_{x_{ij}} \frac{b_{i+1/2,j}}{\xi_{z_j}} + \frac{1}{4\xi_{z_j} h^2} A_{z_{ij}} \frac{b_{i,j+1/2}}{\xi_{x_i}}, \\
A_{c_{i-1,j-1}} &= -\frac{1}{4\xi_{x_i} h^2} B_{x_{ij}} \frac{b_{i-1/2,j}}{\xi_{z_j}} + \frac{1}{4\xi_{z_j} h^2} A_{z_{ij}} \frac{b_{i,j-1/2}}{\xi_{x_i}},
\end{aligned}
\tag{B-3}
$$

The coefficients of submatrices $\mathbf{B_c}$, $\mathbf{C_c}$, and $\mathbf{D_c}$ in system 6 can be inferred easily from those of submatrix $\mathbf{A_c}$ by substituting the coefficients $A_{c_{ij}}$:

- $-A_x$ by C_x, E_x, G_x for submatrices $\mathbf{B_c}$, $\mathbf{C_c}$, $\mathbf{D_c}$, respectively
- $-B_x$ by D_x, F_x, H_x for submatrices $\mathbf{B_c}$, $\mathbf{C_c}$, $\mathbf{D_c}$, respectively
- $-A_z$ by C_z, E_z, G_z for submatrices $\mathbf{B_c}$, $\mathbf{C_c}$, $\mathbf{D_c}$, respectively
- $-B_z$ by D_z, F_z, H_z for submatrices $\mathbf{B_c}$, $\mathbf{C_c}$, $\mathbf{D_c}$, respectively.

APPENDIX C

DISPERSION ANALYSIS

For the RS stencil, we obtain for a_{11}, a_{12}, a_{21}, and a_{22}

$$
\begin{aligned}
a_{11} &= \frac{1}{2}\cos\left(\frac{2\pi}{G}(\cos\phi - \sin\phi)\right)(A_x - B_x - A_z + B_z) \\
&\quad + \frac{1}{2}\cos\left(\frac{2\pi}{G}(\cos\phi + \sin\phi)\right)(A_x + B_x + A_z + B_z) \\
&\quad + \cos\left(\frac{2\pi}{G}\cos\phi\right)(A_x - B_z) + \cos\left(\frac{2\pi}{G}\sin\phi\right)(-A_x + B_z) - (A_x + B_z),
\end{aligned}
$$

$$
\begin{aligned}
a_{12} &= \frac{1}{2}\cos\left(\frac{2\pi}{G}(\cos\phi - \sin\phi)\right)(C_x - D_x - C_z + D_z) \\
&\quad + \frac{1}{2}\cos\left(\frac{2\pi}{G}(\cos\phi + \sin\phi)\right)(C_x + D_x + C_z + D_z) \\
&\quad + \cos\left(\frac{2\pi}{G}\cos\phi\right)(C_x - D_z) + \cos\left(\frac{2\pi}{G}\sin\phi\right) \\
&\quad \times (-C_x + D_z) - (C_x + D_z),
\end{aligned}
$$

$$
\begin{aligned}
a_{21} &= \frac{1}{2}\cos\left(\frac{2\pi}{G}(\cos\phi - \sin\phi)\right)(E_x - F_x - E_z + F_z) \\
&\quad + \frac{1}{2}\cos\left(\frac{2\pi}{G}(\cos\phi + \sin\phi)\right)(E_x + F_x + E_z + F_z) \\
&\quad + \cos\left(\frac{2\pi}{G}\cos\phi\right)(E_x - F_z) + \cos\left(\frac{2\pi}{G}\sin\phi\right)(-E_x + F_z) - (E_x + F_z),
\end{aligned}
$$

and

$$
\begin{aligned}
a_{22} &= \frac{1}{2}\cos\left(\frac{2\pi}{G}(\cos\phi - \sin\phi)\right)(G_x - H_x - G_z + H_z) \\
&\quad + \frac{1}{2}\cos\left(\frac{2\pi}{G}(\cos\phi + \sin\phi)\right)(G_x + H_x + G_z + H_z) \\
&\quad + \cos\left(\frac{2\pi}{G}\cos\phi\right)(G_x - H_z) + \cos\left(\frac{2\pi}{G}\sin\phi\right) \\
&\quad \times (-G_x + H_z) - (G_x + H_z).
\end{aligned}
\tag{C-1}
$$

For the CS stencil, we obtain

$$
\begin{aligned}
a_{11} &= 2\cos\left(\frac{2\pi}{G}\cos\phi\right)A_x + 2\cos\left(\frac{2\pi}{G}\sin\phi\right)B_z - 2(A_x + B_z) \\
&\quad + 0.5\cos\left(\frac{2\pi}{G}(\cos\phi + \sin\phi)\right)(B_x + A_z) \\
&\quad - 0.5\cos\left(\frac{2\pi}{G}(\cos\phi - \sin\phi)\right)(B_x + A_z),
\end{aligned}
$$

$$
\begin{aligned}
a_{22} &= 2\cos\left(\frac{2\pi}{G}\cos\phi\right)C_x + 2\cos\left(\frac{2\pi}{G}\sin\phi\right)D_z - 2(C_x + D_z) \\
&\quad + 0.5\cos\left(\frac{2\pi}{G}(\cos\phi + \sin\phi)\right)(D_x + C_z) \\
&\quad - 0.5\cos\left(\frac{2\pi}{G}(\cos\phi - \sin\phi)\right)(D_x + C_z),
\end{aligned}
$$

$$
\begin{aligned}
a_{12} &= 2\cos\left(\frac{2\pi}{G}\cos\phi\right)E_x + 2\cos\left(\frac{2\pi}{G}\sin\phi\right)F_z - 2(E_x + F_z) \\
&\quad + 0.5\cos\left(\frac{2\pi}{G}(\cos\phi + \sin\phi)\right)(F_x + E_z)
\end{aligned}
$$

$$- 0.5 \cos\left(\frac{2\pi}{G}(\cos\phi - \sin\phi)\right)(F_x + E_z),$$

and

$$a_{21} = 2\cos\left(\frac{2\pi}{G}\cos\phi\right)G_x + 2\cos\left(\frac{2\pi}{G}\sin\phi\right)H_z - 2(G_x + H_z) + 0.5\cos\left(\frac{2\pi}{G}(\cos\phi + \sin\phi)\right)(H_x + G_z) - 0.5\cos\left(\frac{2\pi}{G}(\cos\phi - \sin\phi)\right)(H_x + G_z). \quad \text{(C-2)}$$

REFERENCES

Alkhalifah, T., 1998, Acoustic approximations for processing in transversely isotropic media: Geophysics, **63**, 623–631.

———, 2000, An acoustic wave equation for anisotropic media: Geophysics, **65**, 1239–1250.

Amestoy, P. R., A. Guermouche, J. Y. L'Excellent, and S. Pralet, 2006, Hybrid scheduling for the parallel solution of linear systems: Parallel Computing, **32**, 136–156.

Anderson, J. E., J. R. Krebs, and D. Hinkley, 2008, Source near the free-surface boundary: Pitfalls for elastic finite-difference seismic simulation and multigrid waveform inversion: 70th Annual Conference & Exhibition, EAGE, Extended Abstracts, WO11.

Bale, R. A., 2007, Phase-shift migration and the anisotropic acoustic wave equation: 69th Annual Conference & Exhibition, EAGE, Extended Abstracts, C021.

Bécache, E., S. Fauqueux, and P. Joly, 2003, Stability of perfectly matched layers, group velocities and anisotropic waves: Journal of Computational Physics, **188**, 399–433.

Ben Hadj Ali, H., S. Operto, and J. Virieux, 2008, Velocity model building by 3D frequency-domain full-waveform inversion of wide-aperture seismic data: Geophysics, **73**, no. 5, VE101–VE117.

Berenger, J.-P., 1994, A perfectly matched layer for absorption of electromagnetic waves: Journal of Computational Physics, **114**, 185–200.

Boudou, F., Y. Le Stunff, J. Arnaud, P. Esquier, A. Kenworthy, P. Whitfield, and C. Soufleris, 2007, Benefits of tilted transverse isotropy (TTI) prestack depth migration for reservoir evaluation offshore West Africa: 69th Annual Conference and Exhibition, EAGE, Extended Abstracts, F018.

Brenders, A. J., and R. G. Pratt, 2007a, Efficient waveform tomography for lithospheric imaging: Implications for realistic 2D acquisition geometries and low frequency data: Geophysical Journal International, **168**, 152–170.

———, 2007b, Full waveform tomography for lithospheric imaging: Results from a blind test in a realistic crustal model: Geophysical Journal International, **168**, 133–151.

Brossier, R., S. Operto, and J. Virieux, 2008, 2D elastic frequency-domain full-waveform inversion for imaging complex onshore structures: 71st Annual Conference and Exhibition, EAGE, Extended Abstracts, U019.

Carcione, J., D. Kosloff, A. Behle, and G. Seriani, 1992, A spectral scheme for wave propagation simulation in 3D elastic-anisotropic media: Geophysics, **57**, 1593–1607.

Carcione, J. M., D. Kosloff, and R. Kosloff, 1988, Wave-propagation simulation in an elastic anisotropic (transversely isotropic) solid: Quarterly Journal of Mechanics and Applied Mathematics, **41**, 319–345.

Charles, S., D. R. Mitchell, R. A. Holt, J. Lin, and J. Mathewson, 2008, Data-driven tomographic velocity analysis in tilted transversally isotropic media: A 3D case history from the Canadian foothills: Geophysics, **73**, no. 5, VE261–VE268.

Coutant, O., J. Virieux, and A. Zollo, 1995, Numerical source implementation in a 2D finite difference scheme: Bulletin of the Seismological Society of America, **85**, 1507–1512.

Drossaert, F. H., and A. Giannopoulos, 2007, A nonsplit complex frequency-shifted PML based on recursive integration for FDTD modeling of elastic waves: Geophysics, **72**, no. 2, T9–T17.

Duveneck, E., P. Milcik, P. M. Bakker, and C. Perkins, 2008, Acoustic VTI wave equations and their application for anisotropic reverse-time migration: 78th Annual International Meeting, SEG, Expanded Abstracts, 2186–2190.

Erlangga, Y. A., and F. J. Herrmann, 2008, An iterative multilevel method for computing wavefields in frequency-domain seismic inversion: 78th Annual International Meeting, SEG, Expanded Abstracts, 1956–1960.

Fletcher, R., X. Du, and P. J. Fowler, 2008, A new pseudo-acoustic wave equation for TI media: 78th Annual International Meeting, SEG, Expanded Abstracts, 2082–2086.

Grechka, V., L. Zhang, and J. W. Rector III, 2004, Shear waves in acoustic anisotropic media: Geophysics, **69**, 576–582.

Helbig, K., 1994, Foundations of anisotropy for exploration seismic: Pergamon Press.

Hu, F. Q., 2001, A stable, perfectly matched layer for linearized Euler equations in unsplit physical variables: Journal of Computational Physics, **173**, 455–480.

Hustedt, B., S. Operto, and J. Virieux, 2004, Mixed-grid and staggered-grid finite difference methods for frequency domain acoustic wave modelling: Geophysical Journal International, **157**, 1269–1296.

Jo, C. H., C. Shin, and J. H. Suh, 1996, An optimal nine-point, finite-difference, frequency-space 2D scalar extrapolator: Geophysics, **61**, 529–537.

Jones, K., M. Warner, and J. Brittan, 1999, Anisotropy in multi-offset deep-crustal seismic experiments: Geophysical Journal International, **138**, 300–318.

Komatitsch, D., C. Barnes, and J. Tromp, 2000, Simulation of anisotropic wave propagation based upon a spectral element method: Geophysics, **65**, 1251–1260.

Komatitsch, D., and R. Martin, 2007: Geophysics, **72**, no. 5, SM155–SM167.

Lesage, A. C., H. Zhou, M. Araya-Polo, J. M. Cela, and F. Ortigosa, 2008, 3D reverse-time migration with hybrid finite difference-pseudospectral method: 78th Annual International Meeting, SEG, Expanded Abstracts, 2257–2260.

Luo, Y., and G. T. Schuster, 1990, Parsimonious staggered grid finite-differencing of the wave equation: Geophysical Research Letters, **17**, 155–158.

Mallick, S., and L. N. Frazer, 1987, Practical aspects of reflectivity modeling: Geophysics, **52**, 1355–1364.

Marfurt, K., 1984, Accuracy of finite-difference and finite-elements modeling of the scalar and elastic wave equation: Geophysics, **49**, 533–549.

Nihei, K. T., and X. Li, 2007, Frequency response modelling of seismic waves using finite difference time domain with phase sensitive detection (TD-PSD): Geophysical Journal International, **169**, 1069–1078.

Okaya, D., and T. McEvelly, 2003, Elastic wave propagation in anisotropic crustal material possessing arbitrary internal tilt: Geophysical Journal International, **153**, 344–358.

Operto, S., A. Ribodetti, M. Grini, and J. Virieux, 2007a, Mixed-grid finite-difference frequency-domain viscoacoustic wave modeling in 2D TTI anisotropic media: 77th Annual International Meeting, SEG, Expanded Abstracts, 2099–2103.

Operto, S., J. Virieux, P. Amestoy, J. Y. L'Excellent, L. Giraud, and H. Ben Hadj Ali, 2007b, 3D finite-difference frequency-domain modeling of viscoacoustic wave propagation using a massively parallel direct solver: A feasibility study: Geophysics, **72**, no. 5, SM195–SM211.

Payton, R., 1983, Elastic wave propagation in transversely isotropic media: Martinus Nijhoff Publ.

Pratt, R. G., and R. M. Shipp, 1999, Seismic waveform inversion in the frequency domain, Part II: Fault delineation in sediments using crosshole data: Geophysics, **64**, 902–914.

Ravaut, C., S. Operto, L. Improta, J. Virieux, A. Herrero, and P. dell' Aversana, 2004, Multi-scale imaging of complex structures from multi-fold wide-aperture seismic data by frequency-domain full-wavefield inversions: Application to a thrust belt: Geophysical Journal International, **159**, 1032–1056.

Saenger, E. H., and T. Bohlen, 2004, Finite-difference modeling of viscoelastic and anisotropic wave propagation using the rotated staggered grid: Geophysics, **69**, 583–591.

Saenger, E. H., N. Gold, and S. A. Shapiro, 2000, Modeling the propagation of elastic waves using a modified finite-difference grid: Wave Motion, **31**, 77–92.

Sen, M. K., and P. L. Stoffa, 1995, Global optimization methods in geophysical inversion: Elsevier Science Publ. Co., Inc.

Sirgue, L., J. T. Etgen, and U. Albertin, 2008, 3D frequency domain waveform inversion using time domain finite difference methods: 70th Conference and Exhibition, EAGE, Extended Abstracts, F022.

Sirgue, L., and R. G. Pratt, 2004, Efficient waveform inversion and imaging: A strategy for selecting temporal frequencies: Geophysics, **69**, 231–248.

Sourbier, F., A. Haiddar, L. Giraud, S. Operto, and J. Virieux, 2008, Frequency-domain full-waveform modeling using a hybrid direct-iterative solver based on a parallel domain decomposition method: A tool for 3D full-waveform inversion?: 78th Annual International Meeting, SEG, Expanded Abstracts, 2147–2151.

Sourbier, F., S. Operto, J. Virieux, P. Amestoy, and J. Y. L'Excellent, 2009a, FWT2D: A massively parallel program for frequency-domain full-waveform tomography of wide-aperture seismic data — Part 1: Algorithm: Computers & Geosciences, **35**, 487–495.

———, 2009b, FWT2D: A massively parallel program for frequency-domain full-waveform tomography of wide-aperture seismic data — Part 2: Numerical examples and scalability analysis: Computers & Geosciences, **35**, 496–514.

Stekl, I., and R. G. Pratt, 1998, Accurate viscoelastic modeling by frequency-domain finite difference using rotated operators: Geophysics, **63**, 1779–1794.
Thomsen, L. A., 1986, Weak elastic anisotropy: Geophysics, **51**, 1954–1966.
Toksöz, M. N., and D. H. Johnston, 1981, Seismic wave attenuation: SEG.
Tsvankin, I., 2001, Seismic signatures and analysis of reflection data in anisotropic media: Elsevier Science Publ. Co., Inc.
Virieux, J., 1984, SH-wave propagation in heterogeneous media: Velocity-stress finite-difference method: Geophysics, **49**, 1259–1266.
———, 1986, P-SV wave propagation in heterogeneous media: Velocity-stress finite-difference method: Geophysics, **51**, 889–901.
Zhang, L., J. Rector III, and G. Hoversten, 2005, Finite-difference modelling of wave propagation in acoustic tilted TI media: Geophysical Prospecting, **53**, 843–852.
Zhou, H., G. Zhang, and R. Bloor, 2006, An anisotropic acoustic wave equation for modeling and migration in 2D TTI media: 76th Annual International Meeting, SEG, Expanded Abstracts, 194–198.